2015-07-01

Comparing Theory and Experiment for Analyte Transport in the First Vacuum Stage of the Inductively Coupled Plasma Mass Spectrometer

Matthew R. Zachreson
Brigham Young University - Provo

Comparing Theory and Experiment for Analyte Transport in the First Vacuum Stage of the Inductively Coupled Plasma Mass Spectrometer

Matthew R. Zachreson

A dissertation submitted to the faculty of
Brigham Young University
in partial fulfillment of the requirements for the degree of

Doctor of Philosophy

Ross L. Spencer, Chair
Paul B. Farnsworth
Grant W. Hart
Bryan G. Peterson
Gus L.W. Hart

Department of Physics and Astronomy

Brigham Young University

July 2015

ABSTRACT

Comparing Theory and Experiment for Analyte Transport in the First Vacuum Stage of the Inductively Coupled Plasma Mass Spectrometer

Matthew R. Zachreson
Department of Physics and Astronomy, BYU
Doctor of Philosophy

The inductively coupled plasma mass spectrometer (ICP-MS) has been used in laboratories for many years. The majority of the improvements to the instrument have been done empirically through trial and error. A few fluid models have been made [1], which have given a general description of the flow through the mass spectrometer interface. However, due to long mean free path effects and other factors, it is very difficult to simulate the flow details well enough to predict how changing the interface design will change the formation of the ion beam.

Towards this end, Spencer et al. [2–4] developed FENIX, a direct simulation Monte Carlo algorithm capable of modeling this transitional flow through the mass spectrometer interface, the transitional flow from disorganized plasma to focused ion beam. Their previous work [2–4] describes how FENIX simulates the neutral ion flow.

While understanding the argon flow is essential to understanding the ICP-MS, the true goal is to improve its analyte detection capabilities. In this work, we develop a model for adding analyte to FENIX and compare it to previously collected experimental data.

We also calculate how much ambipolar fields, plasma sheaths, and electron-ion recombination affect the ion beam formation.

We find that behind the sampling interface there is no evidence of turbulent mixing. The behavior of the analyte seems to be described simply by convection and diffusion. Also, ambipolar field effects are small and do not significantly affect ion beam formation between the sampler and skimmer cones.

We also find that the plasma sheath that forms around the sampling cone does not significantly affect the analyte flow downstream from the skimmer. However, it does thermally insulate the electrons from the sampling cone, which reduces ion-electron recombination.

We also develop a model for electron-ion recombination. By comparing it to experimental data, we find that significant amounts of electron-ion recombination occurs just downstream from the sampling interface.

Keywords: inductively coupled plasma mass spectrometry, gas flow simulation, direct-simulation Monte Carlo, DSMC, collisional-radiative recombination, ambipolar electric fields, plasma sheaths

ACKNOWLEDGMENTS

First, I would like to acknowledge the U.S. Department of Energy and the BYU Department of Physics and Astronomy for funding this research. I would also like to acknowledge all the help and support that I received from my advisor, Dr. Ross Spencer. Without his contributions and assistance this dissertation would not be possible. Finally, I would like to thank my wife, Kamee Zachreson, for all of her support and encouragement, especially through all the late nights and long hours it took to put into writing this dissertation. I could not have done it without her.

Contents

Table of Contents iv
List of Figures vi
List of Tables ix
1 Introduction 1

1
1.1 ICP-MS . . . 1
1.2 Free Jet Expansions . . . 2
1.3 FENIX . . . 4

2 Adding Analyte to FENIX **6**
2.1 Introduction . . . 6
2.2 Experimental . . . 9
2.2.1 Fluorescence profiling of radial ion distributions . . . 9
2.2.2 ICP operating conditions . . . 11
2.2.3 Analytes . . . 11
2.3 Theoretical . . . 12
2.3.1 FENIX- analyte addition . . . 12
2.3.2 Convection-diffusion Model . . . 15
2.4 Results and discussion . . . 19
2.4.1 Comparison to Upstream Barium Data: Mills' experiments . . . 19
2.4.2 Comparison of Upstream and Downstream Analyte Profiles . . . 20
2.5 Conclusion . . . 29

3 Ambipolar Electric Fields **32**
3.1 Introduction . . . 32
3.2 Theoretical Model . . . 33
3.3 Results . . . 34
3.4 Conclusion . . . 40

4 Plasma Sheaths **41**
4.1 Introduction . . . 41
4.2 Theory . . . 42

4.2.1 Collisional Sheath Model 42
4.2.2 FENIX 44
4.3 Results 46
4.4 Conclusions 52

5 Simulating Electron/Ion Recombination **53**
5.1 Introduction 53
5.2 Analyzing Macedone and Farnworth's data 55
5.2.1 Removing experimental background 55
5.2.2 Conservation of Mass 57
5.3 Theoretical Model 64
5.3.1 Relating Ion, Atom, and FENIX densities 64
5.3.2 Calculating Ion Density and Electron Temperature 66
5.4 Results and Discussion 69
5.4.1 Calculating K_r from the experiment. 69
5.4.2 General recombination properties 71
5.5 Conclusion 75

Bibliography **76**

List of Figures

1.1 Schematic of an ICP-MS. Horizontal spacing is not drawn to scale. 2

1.2 Diagram of a “free jet" expansion. 3

2.1 Region simulated by FENIX. 8

2.2 Regions covered by Mills’ experiment and by the work presented in this paper. . . 10

2.3 Streamlines of the argon flow in the simulated region obtained from FENIX. 17

2.4 Axial (a) and radial (b,c) density profiles taken from FENIX and Mills’ experimental data [16]. 21

2.5 The upstream experimental density profiles together with the theoretical profiles given to FENIX. 22

2.6 FENIX radial density profiles compared to the experimental profiles at $Z = 10$ mm downstream from the sampling cone. 23

2.7 Mills’ end-on data compared to cross sections of his side-on density data for barium ions at a 1. 25

2.8 FENIX’s radial density profiles for both Ca^+ (a) and Ba^+ (b) at $Z = 10$ mm compared to the results of the convective-diffusive model. 27

2.9 Experimental and FENIX simulation results at $Z = 10$ mm downstream from the sampler for Ca^+ and Ba^+. 30

3.1 The electron temperature used to estimate the ambipolar fields. 34
3.2 The radial velocities for barium (Fig. a) and calcium (Fig. b) 1 mm downstream from the sampling cone. 35
3.3 The radial velocities for barium (Fig. a) and calcium (Fig. b) 5 mm downstream from the sampling cone. 36
3.4 The radial velocities for barium (Fig. a) and calcium (Fig. b) 10 mm downstream from the sampling cone. 36
3.5 Axial velocities for barium (Fig. a) and calcium (Fig. b) on axis. 37
3.6 Analyte densities along the centerline of the expansion. 38
3.7 Radial density profiles for barium 10 mm behind the sampling cone. 38
3.8 Radial density profiles for calcium 10 mm behind the sampling cone. 39
3.9 Analyte radial densities at 10 mm without ambipolar fields compared to ambipolar fields shifted to a different position so that they match the no field densities. 39

4.1 Plasma sheath forming against a conducting wall. 42
4.2 Converged electric field solution compared to the scaled ambipolar field approximation. 46
4.3 Radial plot of the electric field formed by the sheath in the center of the sampling orifice. 47
4.4 Argon ion density overlaid with the streamlines of the flow. 48
4.5 Radial plot of the electron/ion density halfway through the sampling orifice. 49
4.6 Radial plot of the electron/ion density halfway through the sampling orifice, enlarged to show the difference in electron and ion densities near the sampler surface. 50
4.7 Plot of the argon neutral and ion densities. 51

4.8 Plot of what the electron temperature would be if there were no sheath at the beginning of the sampler, 1/1000 of the way into the sampler, and 1/200 of the way into the sampler. 52

5.1 Macedone's [17] normalized data. 54

5.2 Radial plot of two Gaussian density distributions (solid). 56

5.3 Graph (a) shows Macedone's normalized ion and atom signals at 1100 W divided by the on-axis calcium density produced by FENIX. 58

5.4 Plots of Macedone's data with the ion signal background removed. 59

5.5 The result of least squares fitting to the total calcium density (Eq. 5.5). 61

5.6 The percentage of calcium that is ionized as a function of downstream position. . . 62

5.7 Graph showing $G(z)$, the function that scales the experimental data to an on-axis density. 63

5.8 Macedone's data converted into on-axis densities using S and G. 64

5.9 The range of possible electron densities and temperatures that will satisfy the 1-2 mm average recombination rates of Table [5.2]. 70

5.10 The geometry scaled experimental data vs the on-axis densities calculated using Eqs. 5.16 and (5.19). 72

5.11 Electron temperatures used to create Fig. 5.10. 73

5.12 Electron densities used to create Fig. 5.10. 73

5.13 The net ionization/recombination rate, calculated using the electron temperature and density from Figs. 5.11 and 5.12. 74

List of Tables

2.1 ICP and vacuum chamber operating conditions. 12

2.2 The values of the fitting parameters η, ν, and β used in the collision integral in Eq. 2.6, of each ion colliding with argon. 14

5.1 Ion and atom signals measured by Macedone and Farnsworth just upstream from the sampling cone. 61

5.2 Recombination rates calculated by combining FENIX with Macedone's data. . . . 70

Chapter 1

Introduction

1.1 ICP-MS

The inductively coupled plasma mass spectrometer (ICP-MS) has been used in laboratories for many years. It features spectacular analytical sensitivity, high speed, precision and low detection limits. It is capable of detecting metals as low as one part in 10^{15}. It is used in many fields such as the pharmaceutical industry to detect inorganic impurities, in industrial plants to monitor worker's exposure to heavy metals, and to detect single nanoparticles.

The ICP-MS (see Fig. 1.1) analyzes a sample by first introducing it into an $\sim$8000 K argon torch to be ionized. The ionized sample and the background argon then enter into a vacuum stage through the sampling cone, where they undergo a free jet expansion, which makes an excellent ion beam source. [5, 6] The center of the jet continues through a skimmer cone to create a rough ion beam, which then has the free electrons removed by an ion lens. From there, the background neutrals must be removed from the beam. The manner in which the neutrals are removed varies from device to device, but usually involves bending the ion beam in some way so that the ions are redirected to a detector and the neutrals continue onward without bending. Once in the detector,

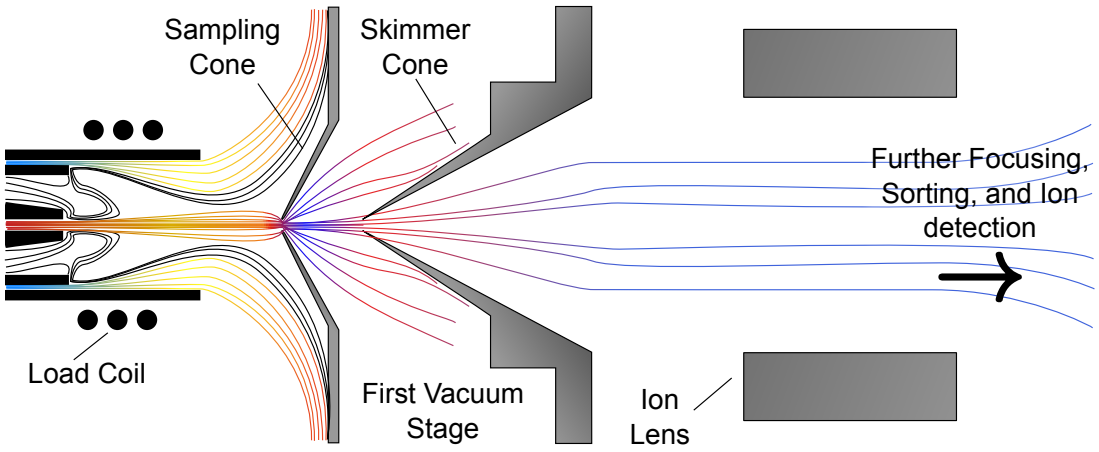

Figure 1.1 Schematic of an ICP-MS. Horizontal spacing is not drawn to scale. To get a sense of scale, the tip of the sampling cone is usually 10 to 15 mm away from the load coil. The sampler and skimmer tips are around 10 mm apart, with the Ion lens sitting 2-4 cm behind the skimmer tip. The sampler and skimmer orifices are both around 1 mm in diameter.

an electric quadrupole then sorts the focused ion beam by the particles' charge to mass ratio.

The efficiency of the ICP-MS is very dependent on the flow structure of the free jet expansion behind the sampling cone and how it forms the ion beam. Understanding the beam formation process is key to improving the performance of the ICP-MS.

1.2 Free Jet Expansions

A jet freely expanding into a vacuum was first described by Owen and Thornhill [7]. Ashkenas and Sherman expanded the work of Owen and Thornhill and others and created an exhaustive fluid model of the expansion. [8] (see Fig. 1.2) This model is limited in the fact that it was created using inviscid flow theory. Inviscid flow theory is invalid when the mean free path is $\sim$0.1% of a characteristic distance of the flow, such as the nozzle radius, since inviscid flow theory assumes that the mean free path is very small compared to the features of flow being described. It also ignores viscous effects, such as boundary layers.

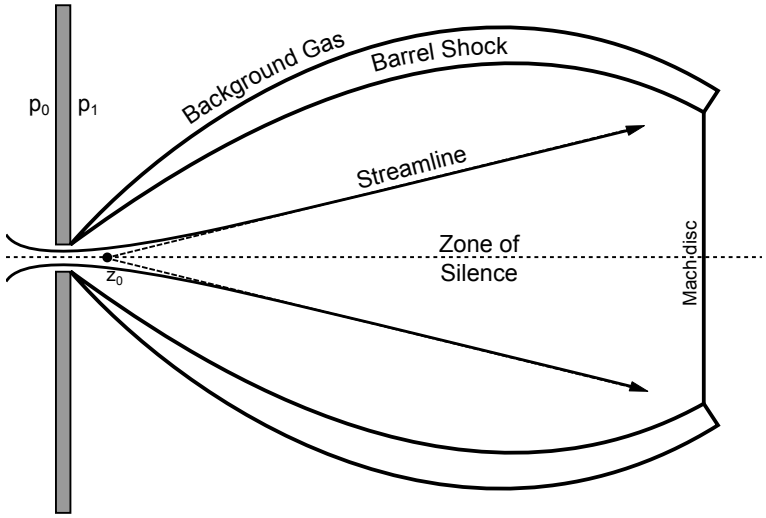

Figure 1.2 Diagram of a “free jet" expansion. Gas is allowed to rapidly expand through a small hole in the boundary between a high pressure p_0 region to a much lower pressure p_1 region. If the pressure difference is great enough, the flow velocities through the hole exceed the speed of sound, and the steady-state “free jet" is formed. This high speed region is called the zone of silence because sound waves cannot propagate upstream. A shock forms at the edge of the expansion where the rapidly expanding gas interacts with the stationary background gas. The result is a rapid decrease in the fluid velocities and an increase in the temperature and density of the gas across the barrel and the Mach disc shock as the pressure in the expanding gas increases to match the background pressure.

To make a more accurate model, Brook and Oman [9] applied the Boltzmann equation to the problem using the BGK method. [10] Later, Hamel and Willis [11] created a better approximation to the Boltzmann equation by using the hypersonic approximation. Knuth and Fisher [12] were able to get past the hypersonic approximation by assuming a single temperature Maxwell-Boltzmann velocity distribution in the expansion. Miller and Andres extended this model using classical scattering theory [13] and Toennies and Winklemann were able to improve it further considering the temperature perpendicular to the flow and the temperature parallel to the flow separately. [14] Toennies and Winklemann's resulting model is more accurate than the fluid model, but is much more cumbersome to use.

Douglas and French were the first to model the free jet expansion through the sampling cone of an ICP-MS. [1, 15] They applied the fluid methods of Ashkenas and Sherman directly to the argon flow in the ICP-MS and also created a hemispherical sink model to describe the flow through the sampling cone.

Later, Spencer et al. created a better approximation to the argon flow in the ICP-MS based on data from the direct simulation Monte Carlo (DSMC) code FENIX. [2–4] Not only is FENIX more accurate than the fluid models, but it is more robust than the Boltzmann equation models.

1.3 FENIX

Previous to this work, Spencer et al. used FENIX to calculate the neutral argon flow through the ICP-MS sampler and skimmer interface. While this information is invaluable, in order to truly understand the analyte extraction process, the analyte entrained in the argon flow must be modeled. This dissertation focuses on what can be learned from modeling the analyte along with the argon. Chapter 2 primarily deals with how the analyte is simulated and how it compares to experimental data. Chapters 3 and 4 discuss the effects of ambipolar fields and plasma sheath formation. Chapter

5 discusses how the atom and ion populations change due to electron ion recombination as the plasma flows through the sampling interface by comparing a theoretical recombination model to experimental data.

Chapter 2

Adding Analyte to FENIX

2.1 Introduction

The freely expanding jet of the first vacuum stage of the ICP-MS makes an excellent ion beam source. The freely expanding jet has been modeled, primarily by fluid methods but also by kinetic methods, for more than 40 years, [5–14] including several models applied specifically to the ICP-MS. [1, 15] Kinetic methods are better because at the low densities of the first vacuum stage the particle mean-free paths can be long enough that fluid methods are unreliable. The Direct-Simulation Monte Carlo method of Bird is especially robust and flexible and has been used to model the neutral argon flow in the ICP-MS. [2–4]

The manner in which analyte ions are transported from the torch region into the first vacuum stage is of particular interest because the loss of these ions limits the effectiveness of the instrument. One important set of experiments that addresses ion transport is that of A. Mills et al. [16] and another is that reported in this paper.

(1) Mills imaged barium ion densities upstream from the sampling cone, both radially and axially. The data of Mills et al. clearly show the outward spread of barium ions as they are formed

near the central axis, then diffuse radially until they are channeled inward in radius by the flow of neutral argon into the sampling cone. Mills' measurements of the barium ion density on the central axis show a sharp decrease in density starting well upstream from the sampling cone, well before the FENIX simulations and ideal fluid theory predict that the argon density should start to drop. His measurements also show that the ion density decrease is not accompanied by an increase in neutral density. Radial diffusion of the narrow barium density profile should cause such a drop, but detailed calculations are needed to see if the effect is purely diffusive. The FENIX simulation results show that diffusion and convection alone are enough to explain Mills results.

(2) In this paper we also report the measurement of radial profiles of both calcium and barium ions about 1 mm (see Fig. 2.1) upstream from the front of the sampling cone, compared to the measurement of these same ion profiles about 10 mm downstream from the sampling cone. The downstream profiles were, of course, significantly wider in radius than the upstream profiles, and the lighter calcium ions produced a wider profile than the heavier barium ions, as expected. But to understand the measured profile broadening in detail requires a theoretical model. The theoretical model reported here is based on the Direct-Simulation Monte Carlo program FENIX [2–4] and it shows that the measured ion density profiles in the zone of silence agree with the predicted actions of convection and diffusion in the expansion behind the sampling cone. The ambipolar electric field of the ions, which should cause additional radial spreading and increased separation between calcium and barium, is found by the simulation to be too weak to cause significant broadening of the radial profiles. These results mean that the measurements show no analyte spreading due to turbulence near the centerline of the ICP-MS vacuum interface.

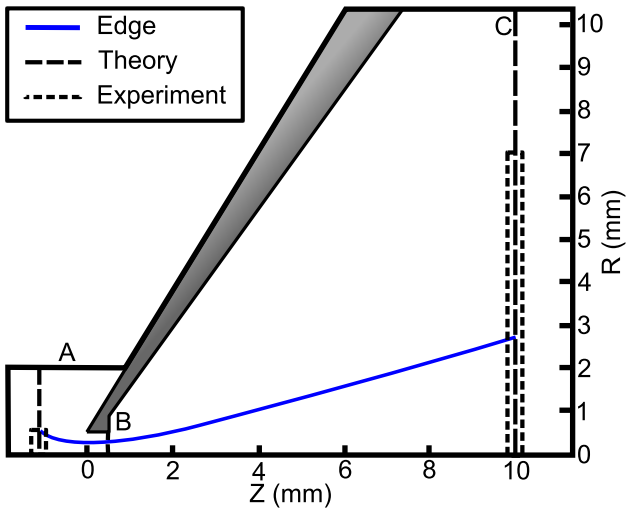

Figure 2.1 Region simulated by FENIX. The dashed lines labeled "Experiment" denote the volumes averaged in the experimental measurements reported in this paper. The dashed lines labeled "Theory" at A and at C denote the radial slices taken in FENIX to compare with the experimental data presented in this paper. The dashed line labeled "Theory" at B shows where the upstream and downstream versions of FENIX were matched. The solid line labeled "Edge" shows how neutral argon fluid flow from FENIX maps the edge of the upstream experimental profile into the first vacuum stage. In all figures, $Z = 0$ is set at the sampler tip and R=0 mm is set at the center axis. Negative Z values are upstream from the sampler tip, positive values are downstream.

2.2 Experimental[1]

2.2.1 Fluorescence profiling of radial ion distributions

Upstream from the sampling cone

The fluorescence excitation and collection optics used to acquire radial profiles of barium and calcium ion distributions upstream from the sampling cone reported in this work were the same as used by Mills, et al. [16] in what is referred to as an "end-on" view. (See Fig. 2.2) Briefly, laser radiation emerging from a 400-μm optical fiber was collimated with a plano-convex singlet lens, then focused to a line with a cylindrical lens. The nominal thickness of the line was 400 μm, dictated by the fiber diameter and the matching focal lengths of the lenses. Over the small field of view in the experiments (1 mm), the laser radiation was treated as a 400 μm thick sheet. The sheet of laser radiation was oriented perpendicular to the plasma axis, immediately upstream from the sampling cone. In practice, the sheet was moved along the plasma axis until scattering was visible on the tip of the sampling cone, and then the sheet was backed away until the scattering disappeared. Mills estimated that the distance between the sheet and the tip of the cone was 0.7 mm, but that value was for a cold instrument. With the plasma on, thermal expansion moved the components, leaving an uncertainty in the position of the sheet with respect to the cone of at least 0.5 mm.

In the work reported here, radial profiles of ion densities immediately upstream from the sampling cone were imaged by optics aligned along the plasma axis, looking upstream through the sampling cone orifice. The gated CCD and imaging optics were isolated from the plasma expansion and from the vacuum by a water-cooled sapphire window. A dye laser was tuned to transitions

[1]The experiment described in this section was carried out by Haibin Ma while he was part of Dr. Paul Farnsworth's research group in the BYU Chemistry department. This section is included in this thesis because a description of the experiment and its results are not currently available elsewhere.

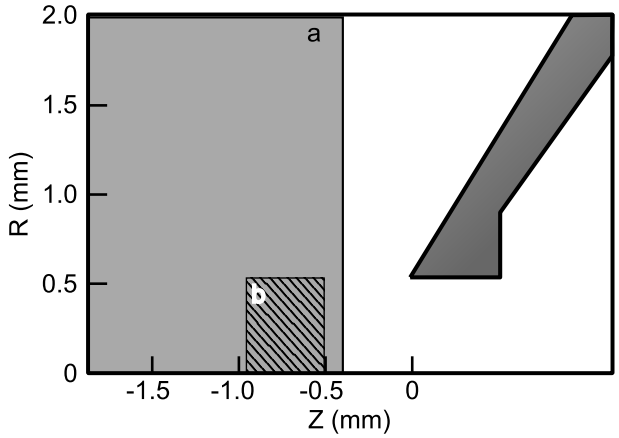

Figure 2.2 Regions covered by Mills' experiment and by the work presented in this paper. Mills took data in two different ways: "side-on", which captured data in region (a) with a resolution of 26 μm, and "end-on", which was taken as described in this paper and which gives the average radial density profile taken over region (b).

at 455.403 nm and 393.37 nm to probe barium and calcium ions, respectively. Fluorescence emission lines were isolated from background with narrow-band interference filters at 614.2 nm for barium and 854.2 nm for calcium. For each final fluorescence image a raw image including both fluorescence and emission signals from 1000 laser shots were summed. A background image of emission only was also recorded under the same conditions, but with the laser blocked, and then the background image was subtracted from the raw image to give the net fluorescence.

Downstream from the sampling cone

Detailed descriptions of the instrumentation used to acquire the downstream radial scans of ion densities are available in earlier publications. [17, 18] To summarize, laser excitation and fluorescence were carried into and out of a vacuum chamber with 0.4-mm optical fibers. The excitation light was focused to an image of the fiber face at an angle of 45 degrees with respect to the axis of the supersonic expansion. Fluorescence was collected in a plane oriented at 90 degrees with respect

to the excitation optics, with the axis of the collection optics also at an angle of 45 degrees with respect to the expansion axis. The probe volume was defined by the overlap of the excitation and emission optical paths, and the baseline spatial resolution in the radial direction was approximately 0.8 mm. Excitation and emission optics were mounted to a rigid frame, which was in turn mounted to a motorized xyz stage. We recorded radial profiles of ion densities by translating the optical assembly in 0.5-mm increments in a direction perpendicular to the expansion axis at a distance of 10 mm downstream from the back end of the sampling cone orifice ($Z = 10$ mm). Fluorescence intensities were recorded at each point with a boxcar averager, and a background recorded using a water blank in place of the analyte was subtracted from each point. The excitation and emission wavelengths for calcium and barium were the same as those used in the upstream measurements. The error bars in both the upstream and downstream data are the standard deviations of three replicate measurements.

2.2.2 ICP operating conditions

The operating conditions for the ICP and vacuum chamber are listed in Table 2.1. The nebulizer gas flows were 1.36 L min^{-1} and 1.33 L min^{-1} for barium and calcium, respectively. The flow nebulizer flow rates were different for the two elements because our goal was to match the upstream profiles to each other as closely as possible, and the vaporization and diffusion properties of barium and calcium were enough different that, at a given flow rate, they did not match.

2.2.3 Analytes

A 10 mg L^{-1} barium solution was prepared from anhydrous barium chloride powder (Spectrum Chemical Mfg. Corp., Gardena, CA). A 25 mg L^{-1} calcium solution was prepared from solid calcium carbonate (AR grade, Mallinckrodt Inc., Paris, KY).

Incident power	1250 Watts
Reflected power	< 5 Watts
Outer gas flow	12 L min^{-1}
Intermediate gas flow	0. 4 L min^{-1}
Sample uptake rate	1 mL min^{-1}
First stage vacuum pressure	$\sim$ 1 Torr
Sampling depth (Distance from load coil to sampling cone)	10 mm

Table 2.1 ICP and vacuum chamber operating conditions.

2.3 Theoretical

Spencer et al. have previously given the details on how FENIX simulates neutral argon flow [2]. Analyte flow is simulated by adding trace particles to the FENIX simulation.

2.3.1 FENIX- analyte addition

The added simulation analyte particles follow the same three basic steps that the argon atoms follow:

1. FENIX advances each particle from time step n to time step $n+1$ through:

$$\mathbf{x}_{n+1} = \mathbf{x}_n + \mathbf{v}_n \tau, \quad \mathbf{v}_{n+1} = \mathbf{v}_n, \tag{2.1}$$

   where $\mathbf{x}$ is the particle position, τ is the time step, and $\mathbf{v}$ is the particle velocity.

2. FENIX assigns each particle to a collision cell.

3. FENIX gives each analyte particle a random chance to collide with the nearest argon neighbor in its collision cell using the collision statistics appropriate to the density and particle

kinetic energies in the cell [19]. Analyte densities are too small for these simulation particles to have good statistics if they are weighted the same as argon neutral particles, and simply increasing the number of simulation argon particles to obtain better analyte statistics is computationally expensive. To correct this problem, two assumptions are made that make it possible to use about the same number of simulation trace particles as simulation argon particles. First, the fact that analyte-argon collisions dominate over analyte-analyte collisions is used. This is done by only allowing simulation analyte particles to collide with simulation argon particles, not with each other. Second, it is assumed that the low-density analyte does not significantly affect the argon flow, so when a simulation trace particle collides with a simulation argon particle, only the simulation trace particle is given a new velocity.

To improve computational efficiency, the simulation volume is divided into two smaller regions (see Fig. 2.1). The first covers the region upstream of the sampling cone, through the sampling cone, and continues on to 1 mm downstream ($Z = -0.8$ mm to $Z = 1.0$ mm). The simulation flow values at the back edge of the sampling cone are then used to seed the second simulation region. This second region includes everything downstream of the sampling cone starting about 0.1 mm before the back edge of the sampler throat. The small volume of overlap between the two regions provides an opportunity to make sure that the transition between the two happens correctly.

The collisional cross sections needed for FENIX can be derived from the momentum-transfer collision integral ($\Omega^{(1,1)}$) data collected by Ellis et al. [20–23] for various ions in neutral argon. The momentum-transfer collision integral is defined to be:

$$\Omega^{(1,1)} = \frac{1}{2(kT)^3} \int_0^\infty \varepsilon^2 e^{-\frac{\varepsilon}{kT}} Q^1 d\varepsilon \tag{2.2}$$

where ε is the relative energy of the particles and Q^1 is defined as

$$Q^1 = 2\pi \int_0^\pi \sin(\theta)\,(1-\cos(\theta))\,\sigma(\varepsilon,\theta) d\theta \tag{2.3}$$

where θ is the scattering angle and σ is the scattering cross section.

	η (10^{-20}m^2)	ν	β (10^{-20}m^2)
K^+	11.3	0.763	9.15
Ca^+	11.2	.842	8.43
Cs^+	11.7	.746	11.5
Ba^+	11.6	0.823	10.6

Table 2.2 The values of the fitting parameters η, ν, and β used in the collision integral in Eq. 2.6, of each ion colliding with argon.

Ellis et al. only collected collision integral data for Ba^+ in Ar up to 2500 K, whereas the simulation reaches temperatures above 5000 K. Also, they collected no collision integral data for Ca^+ in Ar. They did, however, collect collision integral data for several other ions to temperatures above 10000 K. Using this data, it was found that using a fit of the form:

$$\Omega^{(1,1)} = \eta \left(\frac{T}{T_0} \right)^{-\nu} + \beta \tag{2.4}$$

(where T the temperature in K, $T_0 = 4000$ K, and η, ν, β are fitting parameters) and doing a least squares fit only to the data below 2500 K predicts collision integral values up to 6000 K within a few percent for Na^+, K^+, O^+, Rb^+, and Cs^+ in argon gas, all of the ions for which the fit was tested. Therefore, a fit of this form should fairly accurately predict the Ba^+ collision integral up to the needed temperatures.

To estimate the Ca^+ collision integral, for which there is no data, we assume that since potassium and calcium have the same relationship in the periodic table as barium and cesium we may write

$$\frac{\xi_{Ca}}{\xi_K} = \frac{\xi_{Ba}}{\xi_{Cs}}$$

where ξ is one of the fitting parameters (η, ν, or β) and where the subscripts denote the element. This equation is used to determine the unknown calcium ion parameters. The values used for η, ν and α for all four ions can be found in Table 2.2.

FENIX simulates analyte-on-argon collisions using a modified version of the Variable Soft Sphere (VSS) model of Koura et al. [24, 25]. This modified model is equivalent to a differential cross-section $\sigma(\theta)$ given by:

$$\sigma(\theta) = \left(\frac{\alpha A v_r^{-2\nu}}{4\pi} + C \right) \left[\cos^2(\theta/2) \right]^{\alpha - 1}, \tag{2.5}$$

where v_r is the relative speed of the colliding particles and where θ is the center-of-mass scattering angle. A, C and α are fitting parameters, and ν is taken from Eq. 2.4. Note that, in the original VSS cross-section, C is set equal to zero. The cross-section in Eq.(2.5) results in a collision integral of the form

$$\Omega^{(1,1)}(T) = \frac{A\Gamma(3-\nu)}{1+\alpha} \left(\frac{m_r}{2k_B} \right)^{\nu} T^{-\nu} + \frac{8\pi C}{(1+\alpha)\alpha} \tag{2.6}$$

(where m_r is the reduced mass of the colliding particles and k_B is Boltzmann's constant) which has the same general form as Eq. 2.4. Eq. 2.4 allows ν to be directly fitted, but only the ratios $A/(1+\alpha)$ and $C/(1+\alpha)$ to be fitted. A and C cannot be determined independently of α. (The experimental data on viscosity and thermal conduction that would allow α to be determined are not available.) Since α generally falls between 1 and 2.5 [24, 25], tests were made with FENIX at three values of α: 1, 1.66 (the value for Ar-Ar collisions [25]), and 2 with the corresponding values of A and C. The three results differed by less than 1% so the value of α for the analyte in this case seems irrelevant as long as it is set between 1 and 2. In the simulations reported here $\alpha = 1.66$ was used.

2.3.2 Convection-diffusion Model

A particle simulation like FENIX is, in some ways, like an experiment: interesting things happen, but the code often can't tell the user why they happened. To help with interpreting the data from FENIX a fluid model has been developed, written in Matlab. The model assumes that the analyte is primarily entrained in the steady flow field of neutral argon obtained from the FENIX simulation

and then adds diffusion to the continuity equation as follows:

$$n\nabla\cdot\mathbf{v}+\mathbf{v}\cdot\nabla n=\nabla\cdot(D\nabla n) \tag{2.7}$$

where n is the analyte number density, $\mathbf{v}$ is the argon fluid velocity calculated by FENIX and where D is the diffusion coefficient of the ion in neutral argon. Comparing the results of this model to the results of FENIX shows to what extent the more detailed physics of the simulation go beyond convection and diffusion. Note that this is not the same as calculating the flow using the fluid equations. The fluid velocity $\mathbf{v}$ is obtained from FENIX and is then used in the continuity equation, Eq. 2.7.

Consider first the simplest case of convection only ($D=0$). In this case Eq. 2.7 is solved by taking the density gradient in Eq. 2.7 along the streamlines of the flow (see Fig. 2.3) so that Eq. 2.7 becomes:

$$n\nabla\cdot\mathbf{v}+|v|\frac{dn}{ds}=0 \tag{2.8}$$

where ds is distance along the streamlines and where v is the magnitude of the neutral argon velocity. Separating the variables in Eq.(2.8) and integrating along the streamlines gives:

$$n_I(r,z)=n_0(r)\exp\left[-\int\frac{\nabla\cdot\mathbf{v}}{|v|}ds\right] \tag{2.9}$$

where $n_0(r)$ is an initial analyte density profile at a fixed value of z on the FENIX output grid and where $n_I(r,z)$ is the ideal analyte density when diffusion is neglected.

If diffusion is added, Eq. 2.8 becomes:

$$n\nabla\cdot\mathbf{v}+|v|\frac{dn}{ds}=\nabla\cdot(D\nabla n) \tag{2.10}$$

Note that when diffusion is a small effect compared to convection, the spatial second derivative in the diffusion term makes this equation stiff, and hence difficult to solve numerically. A formal solution of this equation may be obtained by integrating along the streamlines as was done in Eq.

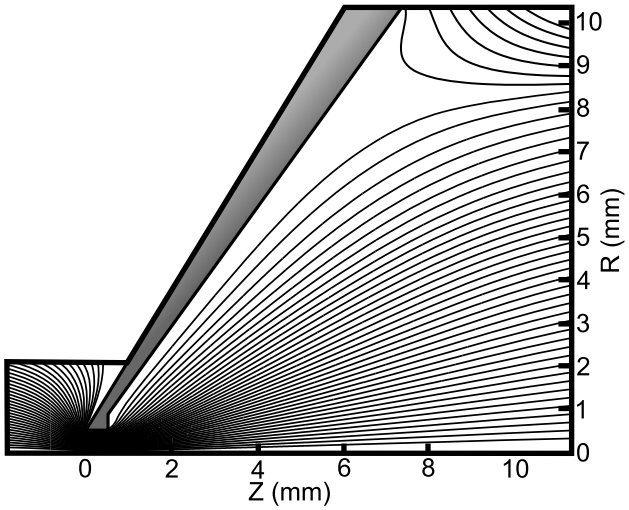

Figure 2.3 Streamlines of the argon flow in the simulated region obtained from FENIX.

2.9:

$$n(r,z) = n_I(r,z)\exp\left[\int \frac{\nabla\cdot(D\nabla n)}{n|v|}ds\right] \tag{2.11}$$

where $n_I(r,z)$ is the solution of Eq. 2.7 and where D is the diffusion coefficient. As long as diffusion does not dominate, this equation may be solved by treating the diffusive term as a small perturbation and then iterating on Eq. 2.11 by successively putting previous iterations into the integral on the right-hand side and performing the integral to obtain a new approximation to $n(r,z)$. The iteration process begins with $n = n_I$, the ideal density from Eq. 2.9, and finishes when $n(r,z)$ satisfies Eq. 2.10. This method fails when fluid velocities are low and D is large, in which case the exponential term in Eq. 2.11 is large and causes iteration to diverge.

Because Eq. 2.11 is stiff it is also necessary to smooth the density profile as iteration proceeds. Derivatives of the density in r and z are taken by fitting a paraboloid to a small section of data, then reading off the fitting coefficients. Then, to suppress numerical instabilities, at each iteration step the density $n(r,z)$ is fitted radially to a sum of two Gaussian profiles. This double Gaussian is chosen because it works well empirically. Note that we also use this fitting function to approximate the upstream experimental density profiles to initiate FENIX. When the iteration has converged we

check to make sure that Eq. 2.10 has actually been solved. We find that it has been, to an accuracy of about 1%.

This numerical procedure is only possible if the diffusion coefficient of each ion in neutral argon is known. The diffusion coefficient D is obtained by first converting the collision integral data collected by Ellis et al. [20–23] into mobility μ using: [20]

$$\mu = \frac{3}{8}\frac{q}{n_{Ar}}\left(\frac{\pi}{2m_r k_B T}\right)^{1/2}\frac{1}{\Omega^{(1,1)}(T)} \tag{2.12}$$

where q is the elementary charge and n_{Ar} is the argon atom number density. The mobility can then be converted to a diffusion coefficient through the Einstein relation:

$$D = \frac{\mu k_B T}{q} \tag{2.13}$$

where μ is the mobility, k_B is Boltzmann's constant, T is the neutral argon temperature, and q is the charge of the ion.

Care must be taken in using a diffusion coefficient in a fluid model when the mean free path is on the order of the size of the region being studied. The problem is that diffusion is limited by the largest possible particle flux, so that for large density gradients the Fick's law flux $\Gamma = -D\nabla n$ can predict unphysically large diffusive fluxes. In order for the diffusion term in Eq. 2.10 to be physical, the diffusion flux Γ must be less than the thermal flux which is on the order of nv_{th}, where $v_{th} = \sqrt{k_B T/m}$. Γ is given by:

$$\Gamma = -D\nabla n \sim -\frac{Dn}{L} \tag{2.14}$$

where L is a representative scale length for density variation. In the region upstream of the nozzle and in the zone of silence, Γ is less than 5% of nv_{th}. In the shock zone, however, Γ reaches a significantly larger percentage of nv_{th}, but never exceeds half of nv_{th}. However, in this region, the fluid velocity is high enough that diffusion effects are negligible. This means that the drift diffusion equation (Eq. (2.10)) should be physical when using velocity data supplied by FENIX.

It should also be noted that starting at about $Z = 3$ mm, FENIX shows that the velocity distribution function is not a simple Maxwellian, so the concept of temperature, used in the diffusion coefficient, becomes suspect. As will be shown, however, if we define the temperature in terms of the average particle kinetic energy in the moving frame of the fluid, FENIX and the drift-diffusion model of Eq. 2.7 agree very well.

2.4 Results and discussion

2.4.1 Comparison to Upstream Barium Data: Mills' experiments

The results of Mills et al. [16] present an opportunity to check the accuracy of the FENIX simulation. Mills measured the distribution of barium ions upstream from the sampling cone, making it possible for the simulation to try to match the experimentally-determined evolution of barium density. The radial profile of barium ions 2 mm upstream from the sampling cone ($Z = -2.0$ mm) was loaded into the FENIX simulation and propagated downstream into the sampling cone. Panel (b) in Fig. 2.4 shows the comparison between simulation and experiment at $Z = -1.25$ mm. The agreement is quite good and also significant because the profile at $Z = -1.25$ mm is wider than it would be with convection only.

The relatively steep radial density gradient of the barium profile results in significant diffusion, as can be seen in panel (a) of Fig. 2.4. The dashed line shows the axial argon density profile from FENIX at $r = 0$. It can be seen that the argon density only starts to drop because of the accelerated flow into the sampler at about $Z = -0.5$ mm. The experimentally measured barium ion density, however, is dropping steadily as the sampling cone is approached, and Mills et al. also showed that the barium ion decrease was not accompanied by a rise in barium neutrals. The simulation explains this mystery: radial diffusion causes the centerline barium density to drop faster than would be expected from ideal fluid flow. The argon density remains constant longer because it has

no radial gradient and hence does not diffuse.

As seen in panel (a) of Fig. 2.4, at distances closer than 1.25 mm to the sampling cone the experimental method of Mills et al. suffers from signal attenuation because the laser sheet did not extend with full intensity to the tip of the sampling cone. This makes it erroneously appear as if the ion density were dropping more rapidly than the simulation in the approach to the sampling cone. A strong indication that this rapid drop is due to signal attenuation can be found by normalizing both the FENIX radial profile and the experimental profile to their central values at $Z = -0.5$ mm, well inside the apparent attenuation region. As can be seen in panel (c) of Fig. 2.4, the two profiles match very well except in the outer edge.

2.4.2 Comparison of Upstream and Downstream Analyte Profiles

Experimental Results

The upstream experimental density profiles of Sec. 2.2.1 are presented in Fig. (2.5). The two dimensional CCD images were converted to an axially symmetric profile using the following process. First, the center of the distribution was found by taking a density weighted average over all points where the density was greater than 90% of the maximum value. 90% was used because taking a density weighted average over the full image found the center of the sampling orifice, not the center of the distribution. Also the data were too noisy to simply put the center of the distribution at the most intense pixel. Once the center was found, an algorithm collected all of the pixels whose center fell within successively larger rings of equal width, and then computed the average pixel value and standard deviation. The averaged data were then normalized to the peak value. The R positions of the data in Fig. (2.5) are relative to the center of the ring over which the data were averaged. The data points represent the average of three CCD images processed in the described manner. The error bars were calculated by combining the standard deviations of the three different images using Gaussian error propagation.

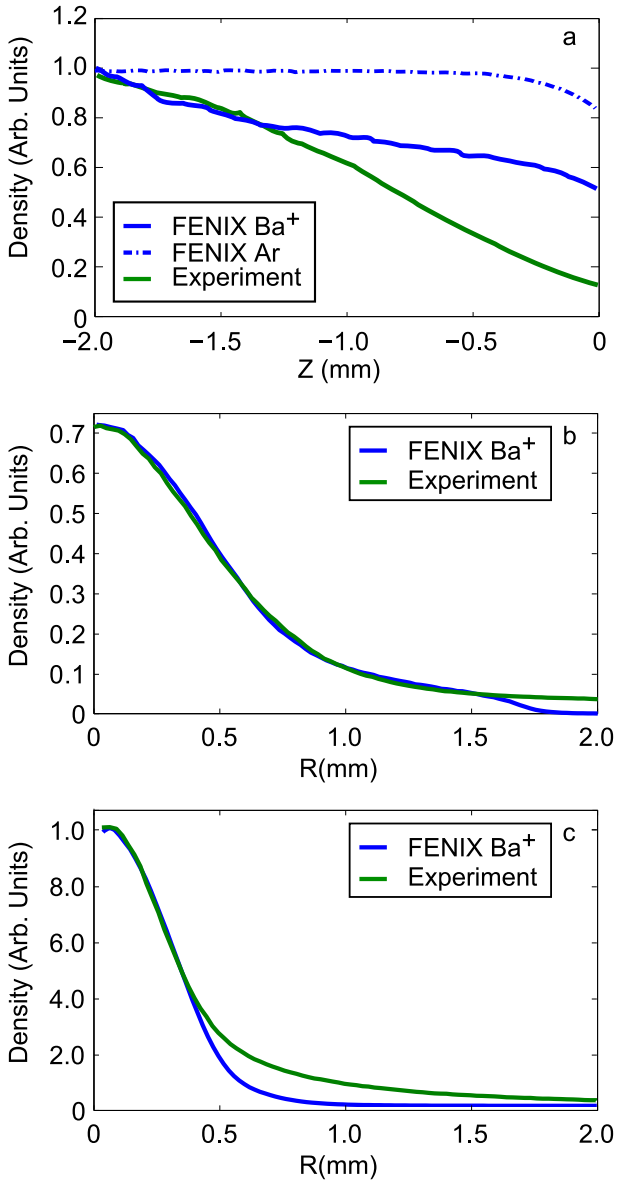

Figure 2.4 Axial (a) and radial (b,c) density profiles taken from FENIX and Mills' experimental data [16]. FENIX was started with the experimental profile at $Z = -2$ mm. Panel (a) shows the axial ion density at R=0. The drop in axial ion density can be explained by diffusion and convection. Note that the argon gas flow does not predict the observed barium density drop. Panel (b) shows the resultant FENIX radial profile compared to the experimental profile at $Z = -1.25$ mm, where the axial densities begin to disagree. Mills reported signal attenuation beginning at $Z = -1.0 \pm 0.5$ mm, which explains why the experimental barium density drops faster than FENIX. (See panel (a)) Panel (c) shows both the FENIX and the experimental radial profiles normalized to unity at the center at $Z = -0.5$ mm, well inside the attenuation region. They match very well, except in the outer edge, indicating that signal attenuation is the reason for the discrepancy seen in panel (a).

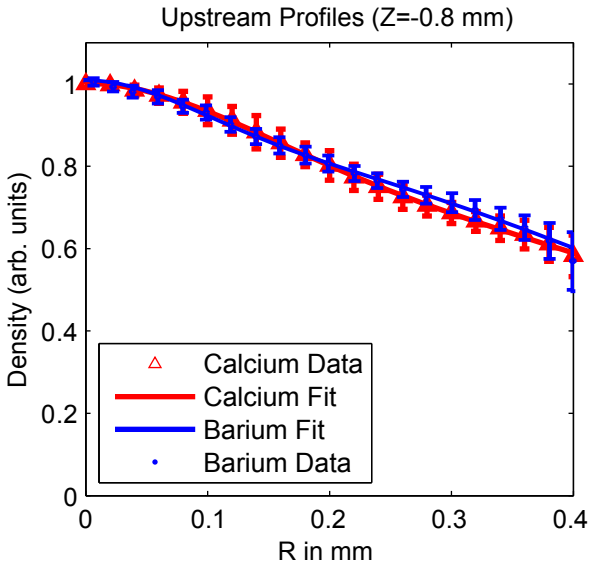

Figure 2.5 The upstream experimental density profiles together with the theoretical profiles given to FENIX: $n(R) = .8713\exp(-R^2/4.4165 \times 10^{-7}) + .1328\exp(-R^2/1.506 \times 10^{-8})$ was used for Ba^+ and $n(R) = .901\exp(-R^2/3.769 \times 10^{-7}) + .099\exp(-R^2/1.815 \times 10^{-8})$ was used for Ca^+, with R in meters.

The downstream density profiles measured as described in Sec. 2.2.1 were taken along a horizontal axis perpendicular to the centerline flow of the ICP at $Z = 10$ mm. In order to facilitate comparison with the results of FENIX, these horizontal profiles were converted to radial profiles by averaging densities at positive and negative values of the horizontal coordinate. These experimental profiles are presented in Fig. (2.6). The results of the FENIX simulation were then used to see if the physical processes of convection and diffusion are sufficient to explain these profiles.

Simulation Starting Profiles

In order for FENIX to simulate the flow of analyte through the sampling cone in the experiments of Sec. 2.4.2 it must be given the radial analyte profile appropriate for the small region labeled (b) in Fig. 2.2. Double Gaussian fits (see the caption of Fig. 2.5) were made to the experimental radial density profiles, taken for barium at a flow rate of 1.36 L min^{-1} and for calcium at a flow

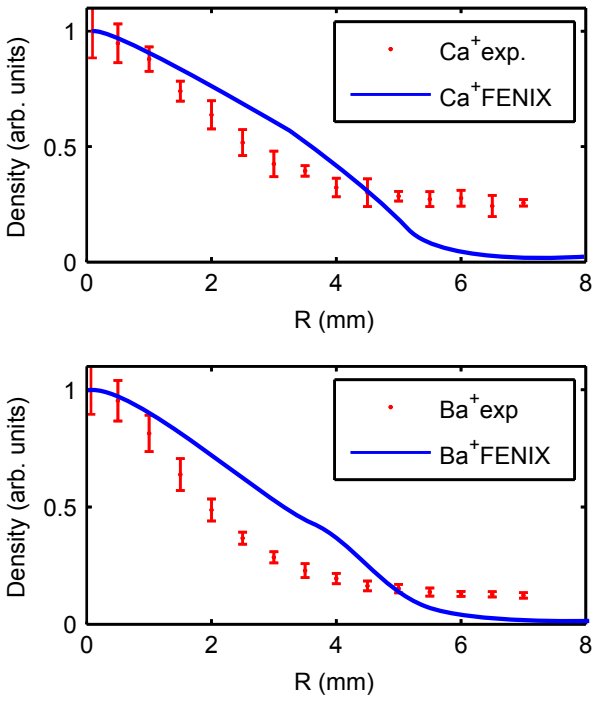

Figure 2.6 FENIX radial density profiles compared to the experimental profiles at $Z =$ 10 mm downstream from the sampling cone. The fine-scale profile data from FENIX have been volume-integrated to mimic the data collection techniques. The barrel shock begins forming at about 2 mm in radius, and is fully formed around 4 mm in radius. [26]

rate of 1.33 L min^{-1}. (See Fig. 2.5) These flow rates were chosen in the experiments because they produce almost identical radial density distributions, making it easier to see the effect of different diffusion rates on the analyte profiles.

The experimental density profiles, however, represent an average density over a region 0.4 mm thick in Z, whereas FENIX has a resolution on the order of a few μm. Therefore, care must be taken in choosing a starting point for the FENIX simulation. The laser sheet was centered at roughly $Z = -0.7$ mm, but the average density from $Z = -0.9$ mm to $Z = -0.5$ mm may not correspond to the density at $Z = -0.7$ mm, therefore it is not prudent to simply start the simulation with the fitted profiles at $Z = -0.7$ mm. In addition, the actual position of the sampling cone is uncertain to within a half-millimeter, or so, because of thermal expansion of the cone assembly. A reasonable starting range can be determined by comparing Mills' "end-on" and "side-on" data. This was done by taking radial cross sections of the "side-on" data, which has a resolution comparable to FENIX's, and finding the axial position where the radial density profile from the "side-on" measurement matches the "end-on" density profile for the same flow rate. (See Fig. 2.7) The axial position of the point where the "side-on" radial density profile agrees with the "end-on" radial profile ranges from $Z = -0.9$ mm to $Z = -0.7$ mm. $Z = -0.8$ mm was the average matching position, so it was used as the axial position of the fits to the radial profiles of Sec. 2.4.2. In general, the "side-on" profiles that matched the "end-on" profiles near $R = 0$ were narrower than the "end-on" profiles at larger R as seen in figure 2.7. This is most likely due to either some effect resulting from averaging the width of the laser sheet or due to some small unaccounted for floor in the experimental signal.

FENIX compared to the convection-diffusion model

To understand the physical effects involved in the transport of analyte through the sampling cone it is helpful to compare the results of FENIX to those of the simple convection-model of Sec.2.3.2. As can be seen in Fig. 2.8, FENIX agrees very well with the convection-diffusion model of Eq.

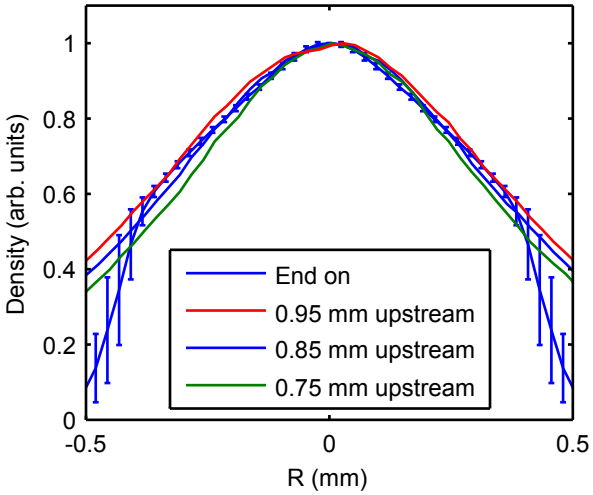

Figure 2.7 Mills' end-on data compared to cross sections of his side-on density data for barium ions at a 1.26 L/m flow rate. 9.5 mm upstream refers to the radial cross section of the side-on density taken at $Z = -9.5$ mm. 8.5 mm upstream and 7.5 mm upstream refer to the radial density profiles at $Z = -0.8$ mm and $Z = -0.9$ mm. End-on is the radial average of Mills' end-on profiles. The error bars are the standard deviation. For this data set, the ideal FENIX starting point would be about $Z = -0.85$ mm. In Mills' measurements for other flow rates, the ideal FENIX starting point ranged from $Z = -0.7$ mm to $Z = -0.9$ mm, with $Z \approx -0.8$mm being the most common. Note: the density drop in the "End-on" profile starting at 0.4 mm in radius is due to the sampling cone windowing the data and is unphysical.

2.11. Panel (a) of this figure shows that the effect of diffusion is significant, since convection alone gives poor agreement. Note also that, once the velocity profile is known (from FENIX with neutral argon and assuming that the ions are entrained in the argon flow in this case), convection and diffusion are sufficient to describe analyte transport. Note also that in this figure the traces for convection and convection-diffusion end at the downstream radial position corresponding to the streamline that connects to the upstream edge of the experimentally-measured radial density profile. The FENIX data that extend beyond that point are the result of extrapolating the upstream radial density profiles in Fig. 2.5 out to a larger radius upstream.

Upstream profiles compared to downstream profiles

With the upstream profiles determined, FENIX can transport them through the sampling cone and into the first vacuum stage where the simulated radial profiles can be compared to those of the experiments of Sec. 2.4.2. To compare the FENIX data to the downstream experimental density profiles, the FENIX data must be integrated over the proper collection volume to reflect the experimental data collection technique. To create the FENIX trace in Fig 2.6, the FENIX data were integrated over a volume that mimics the intersection volume of the excitation laser and the collection optics. The integration volume consists of two cylinders, 0.4 mm in diameter, that intersect at 45 degrees. The integration volume is centered radially at each experimental data point and centered axially at $Z = 10$ mm from the sampling cone tip.

The volume-integrated FENIX profiles are wider than the experimental profiles within the zone of silence. The disagreement could be due to several factors, one of which is the uncertainty in the FENIX axial starting position discussed in Sec. 2.4.2. Moving the starting profiles a few tenths of a millimeter upstream significantly narrows the resulting downstream FENIX radial density profiles. Also, the upstream experimental density profiles of Sec. 2.4.2 may be slightly narrower than what was measured as seen in Fig. 2.7.

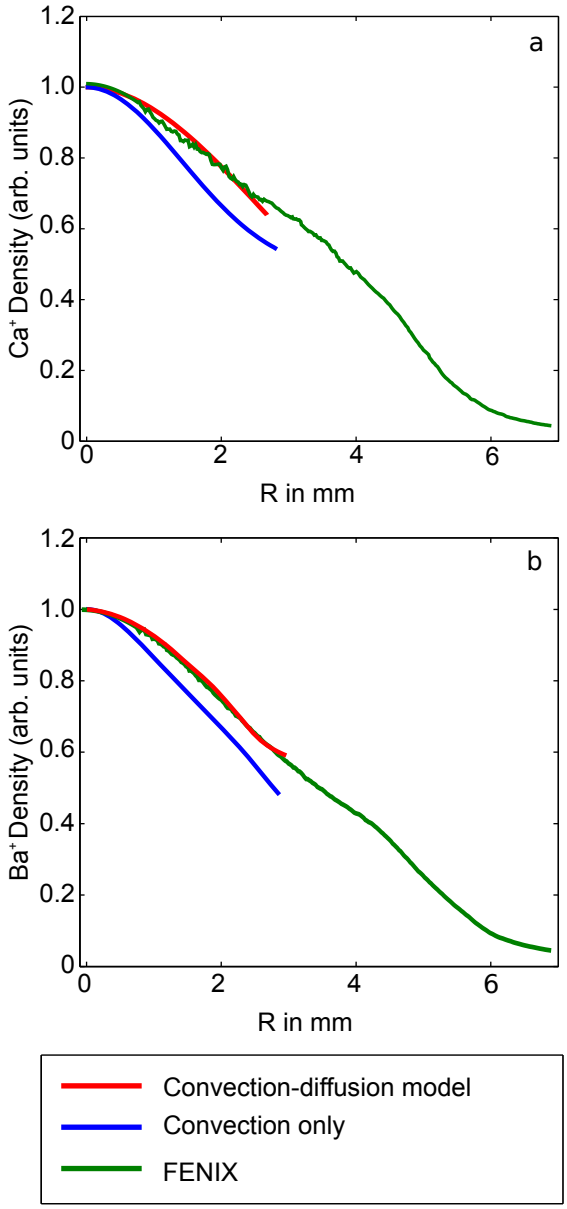

Figure 2.8 FENIX's radial density profiles for both Ca^+ (a) and Ba^+ (b) at $Z = 10$ mm compared to the results of the convective-diffusive model. The convection-only results are included to show the amount that diffusion affects the density profiles. The convection-diffusion profiles stop at the radius obtained by connecting a point at radius $R = 0.4$ mm and $Z = -1.1$ mm to one at $Z = 10$ mm along the argon streamlines (the right-hand edge of the end-on experimental profiles in Fig. 2.5. This upstream point was chosen because the end-on profiles become unphysical at radii beyond this point, see Fig. 2.7). Note that FENIX suffers from poor statistics near $R = 0$ mm because there are hardly any particles in these small volumes near the origin. To correct for this, the FENIX results at less than $R = 0.5$ mm have been fitted to a parabola.

However, The amount that experimental and theoretical density profiles of 2.6 do agree indicates that convection and diffusion are enough to account for the ion transport through the sampling cone near the central axis. In particular, there is no hint of turbulent mixing of the central flow. The sharp drop in the FENIX simulation density profiles at $R = 4$ mm that isn't present in the experimental profiles could be due to several different factors not included in the FENIX simulation. The outer edge of the upstream experimental profiles (near $R = 0.4$ mm) presented in this paper only extends to about 3 mm in radius when propagated to $Z = 10$ mm downstream, so the disagreement may be the result of an extrapolation error when setting FENIX's upstream density profiles. However, density beyond $R = 0.4$ mm was taken in the side-on images of Mills and these profiles agree reasonably with the double-Gaussian fits we use here to start FENIX. Also, at $Z = 10$ mm the barrel shock begins forming at about 2 mm in radius, and is fully formed around 4-5 mm in radius [26], so the disagreement may come from ions present in the first vacuum stage background. However, simply introducing analyte ions at the downstream simulation's outer radial boundary in FENIX does not form the tail seen in the downstream experimental data. Note that particles at the downstream outer radial edge of Fig. 2.3 are rapidly swept downstream outside of the flow separatrix that can be seen in this figure. However, some turbulent mixing may be occurring that is not captured by FENIX. The Reynolds number in the region is only a few hundred, below the turbulent or even the transitional flow regimes, so it is not expected to see turbulence in the model. However, the sampler tip or some other feature may be seeding turbulence in the barrel shock that could only be captured by a fully three dimensional model.

It must be noted that a similar experiment [27] did not detect a floor in the downstream analyte densities at large radius.

Adding an approximate ambipolar electric field [3] widens the FENIX density profile widths at $Z = 10$ mm by less than 2%. The same amount of widening can be seen by taking the density profiles a tenth of a millimeter further downstream. Since the uncertainty in the distance from the

sampling cone measurement points downstream is about a millimeter, the experimental uncertainty is too large to resolve any of the finer details of transport due to ambipolar fields.

There is some electron-ion recombination that occurs for a few millimeters downstream from the sampler cone, [17] but it does not significantly affect the radial density distribution of the ions because the recombination rate is nearly uniform in radius.

Comparing Calcium and Barium

The upstream density profiles for Ca^+ and Ba^+ are nearly identical. (See Fig. 2.5) Their respective flow rates were chosen to ensure this. Downstream, the Ca^+ density profile is significantly wider than the Ba^+ profile. (See Fig. 2.9) This is expected, since Ca^+, as a lighter ion, has a much higher diffusion coefficient than Ba^+. Therefore, FENIX and the experiments of Sec.2.4.2 confirm the ICP-MS's tendency to favor high mass ions.

2.5 Conclusion

Mills et al. [16] observed a decrease in the barium analyte density along the axis near the entrance to the sampling orifice which was faster than expected from ideal fluid flow. FENIX has provided further details about this flow and has shown that this drop in axial barium density is simply caused by diffusion of the peaked analyte density profile. The converging flow into the sampling cone steepens the analyte density further, resulting in even more diffusion. This effect significantly reduces the ion density on axis and reduces the sensitivity of the ICP-MS since only ions on the centerline arrive at the mass analyzer.

In conjunction with the experimental data presented here, FENIX has also shown that convection and diffusion are enough to account for the analyte flow through the sampling orifice of the ICP-MS. However, the experimental data were not accurate enough to determine the strength of

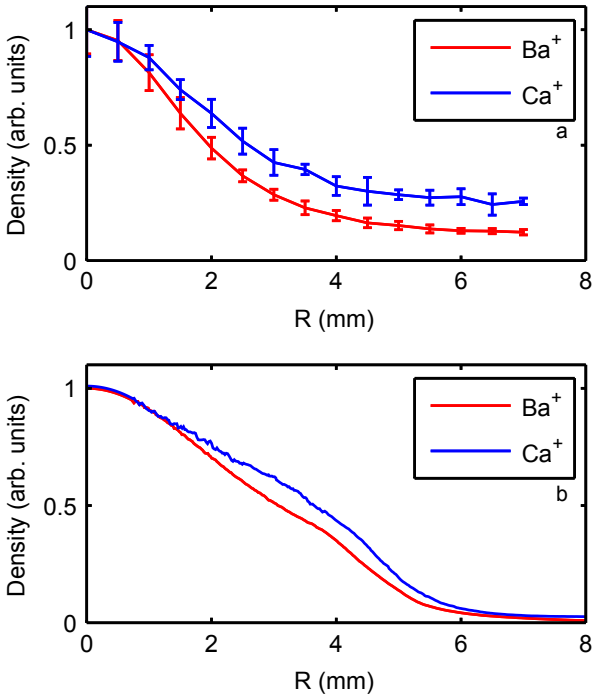

Figure 2.9 Experimental (a) and FENIX simulation (b) results at $Z = 10$ mm downstream from the sampler for Ca^+ and Ba^+.

ambipolar field effects. This agreement between the measured profiles and convection and diffusion means that there is no hint in the experimental results reported here of turbulence near the centerline of the ICP-MS.

Also, the FENIX simulation is unable to account for a floor observed in the experimental analyte densities in the first vacuum stage. Further study is warranted.

Acknowledgment

Work supported by the US Department of Energy, contract DEFG02- 03ER15410.

Chapter 3

Ambipolar Electric Fields

3.1 Introduction

In a plasma, the free electrons have a much higher mobility than any other species. The average speed of a species of particles in a plasma is approximately $v \sim \sqrt{kT/m}$ where k is Boltzmann's constant, T is the temperature, and m is the mass of the species. In a hydrogen plasma, if the electrons and ions are the same temperature, the electrons will be moving over 40 times faster than the ions. In an argon plasma, like the one used by an ICP-MS, the electrons are faster by almost a factor of 300. Because of this, electrons diffuse much faster than ions. Whenever there is a density gradient within a plasma, this difference in diffusive speeds creates a charge imbalance. The charge imbalance in turn creates an electric field. The field slows the electron diffusion, but speeds up the ion diffusion. The electric fields then stabilize when the electrons have slowed sufficiently and the ions have sped up sufficiently to maintain quasi-neutrality. This enhanced diffusion is called ambipolar diffusion or the ambipolar effect. In fluid models, the ambipolar diffusion coefficient (D_A) is given by: [28]

$$D_A = \left(1 + \frac{T_e}{T_i}\right) D \tag{3.1}$$

where D is the normal diffusion coefficient, T_e is the electron temperature, and T_i is the ion temperature. In a plasma $T_e \geq T_i$ almost always, therefore ambipolar field effects will at least double what happens in normal diffusion. In the ICP-MS, upstream from the sampling cone $T_e \approx T_i$. However, downstream from the sampling cone T_e is significantly higher than T_i.

3.2 Theoretical Model

Since FENIX isn't a fluid model, ambipolar field effects cannot be calculated with the ambipolar diffusion coefficient. FENIX simulates electric fields by first loading a static field across the simulation geometry. Then, as the particles are advanced each time step, the electric fields accelerate the charged particles. Therefore, the only requirement for modeling ambipolar with FENIX is to feed FENIX the electric field. The ambipolar electric field $\mathbf{E}$ can be calculated directly by using: [3]

$$\mathbf{E} = -\frac{1}{en_e}\nabla k_B n_e T_e \tag{3.2}$$

where n_e is the electron density, n_0 is the argon neutral density, e is the elementary charge, k_B is Boltzmann's constant, and T_e is the electron temperature. The argon ion density (n_{Ar^+}) is a few orders of magnitude larger than the analyte density. Therefore, the contributions to the electron density from the analyte are negligible. Also, Gamez et al. [29] showed that adding analyte to the argon plasma does not significantly impact the electron densities and temperatures. Therefore, it is safe to assume that $n_e \approx n_{Ar^+}$, turning Eq. 3.2 into:

$$\mathbf{E} \approx -\frac{1}{en_{Ar^+}}\nabla k n_{Ar^+} T_e \tag{3.3}$$

It is very difficult to experimentally measure the electron density or temperature, or the argon ion density. However, the Saha equation predicts that about 0.1% of the argon will be ionized. So, for modeling purposes it is assumed that $n_{Ar^+} = 0.001 n_{Ar}$ where n_{Ar} is the argon neutral density taken from FENIX.

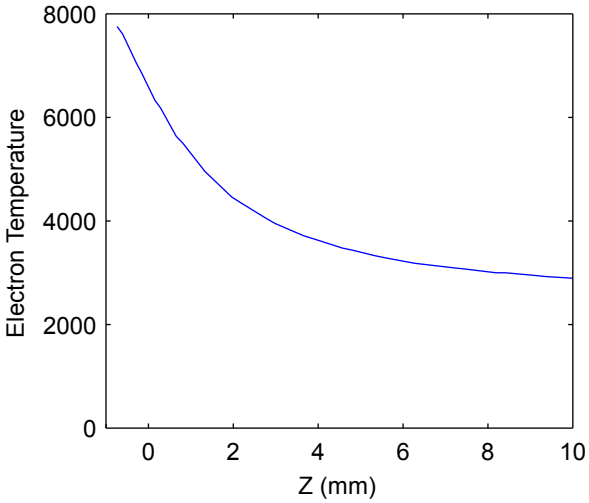

Figure 3.1 The electron temperature used to estimate the ambipolar fields.

The electron temperature for the ambipolar field calculation was taken from Farnsworth et al. [3] and is shown in Fig. 3.1. They found this temperature profile was the best fit for matching experimentally observed ambipolar field effects in a particular experiment.

To make a two-dimensional electron temperature, it is assumed that the expansion is spherical. The argon densities are calculated directly from the argon neutral density data produced by FENIX. For comparison, four FENIX simulations were executed. Two were with barium and calcium without ambipolar fields. The other two simulated barium and calcium with ambipolar fields in place.

3.3 Results

Figs. 3.2, 3.3, and 3.4 show the analyte radial velocities at 1 mm, 5 mm and 10 mm downstream. Near the sampling orifice, the free jet expansion creates large density and temperature gradients, resulting in a large ambipolar field. This can be seen in the increased radial flow velocities of Fig. 3.2. By 5 mm downstream from the sampling cone, the radial ambipolar field is small and it affects

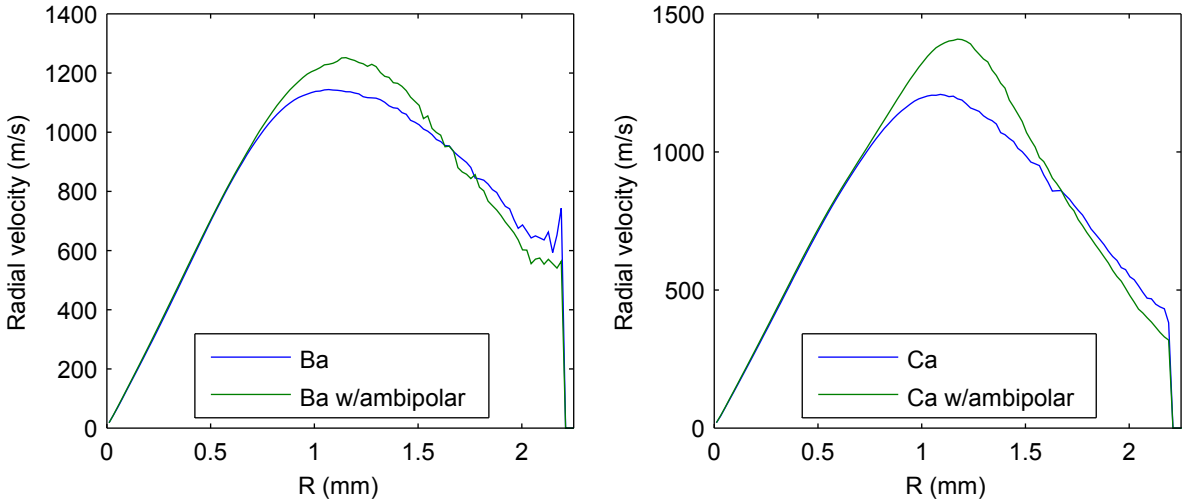

(a) **(b)**

Figure 3.2 The radial velocities for barium (Fig. a) and calcium (Fig. b) 1 mm downstream from the sampling cone.

the radial ion velocities very little, as seen in Figs. 3.3 and 3.4.

Fig. 3.5 shows the flow speeds along the centerline. Notice that in both cases the peak flow with the ambipolar electric fields is noticeably (3%) higher than the analyte flow speeds without it as observed in [3]. In the expansion, where the mean free path is still short, the ions in all four cases are collisionally coupled to the argon neutrals. Then, as the mean free path gets longer, the ambipolar fields accelerate the ions, giving them a greater speed until they encounter the Mach disc at about 15 mm. Through the Mach disc, the argon density increase as it does in the barrel shock. The increase in density results in an ambipolar field that points upstream, resulting in an ion flow speed slower than without the ambipolar field (3% for calcium, less for barium).

The difference between the analyte densities with and without ambipolar fields on axis is about 20% for calcium and 10% for barium. (See Fig. 3.6) A the largest difference can be seen near the end of the zone of silence (Z=10-15 mm). The radial density profiles for barium at 10 mm downstream from the sampling cone are shown in figure 3.7. The differences in barium densities

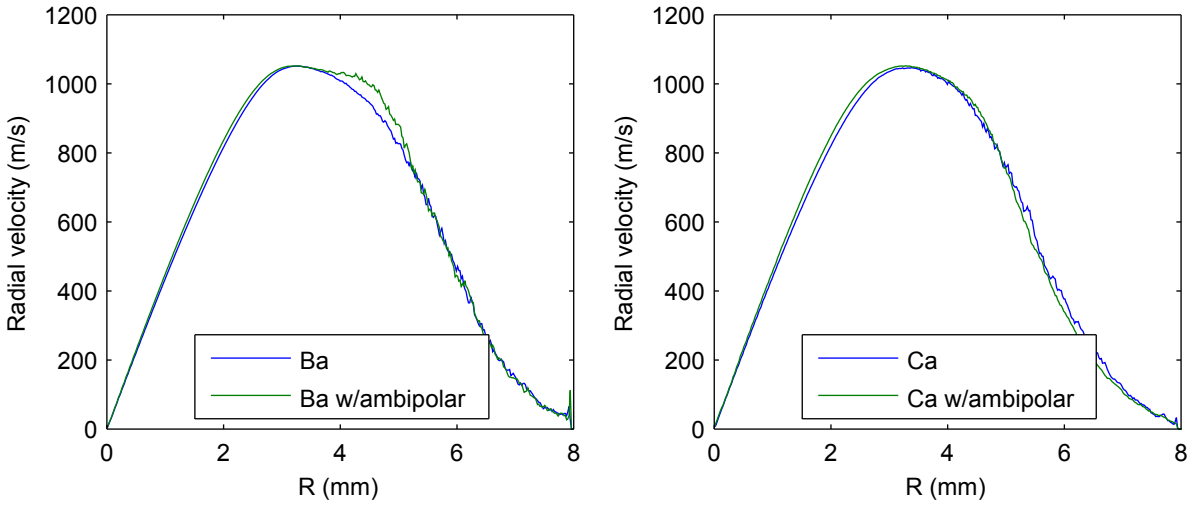

(a) **(b)**

Figure 3.3 The radial velocities for barium (Fig. a) and calcium (Fig. b) 5 mm downstream from the sampling cone.

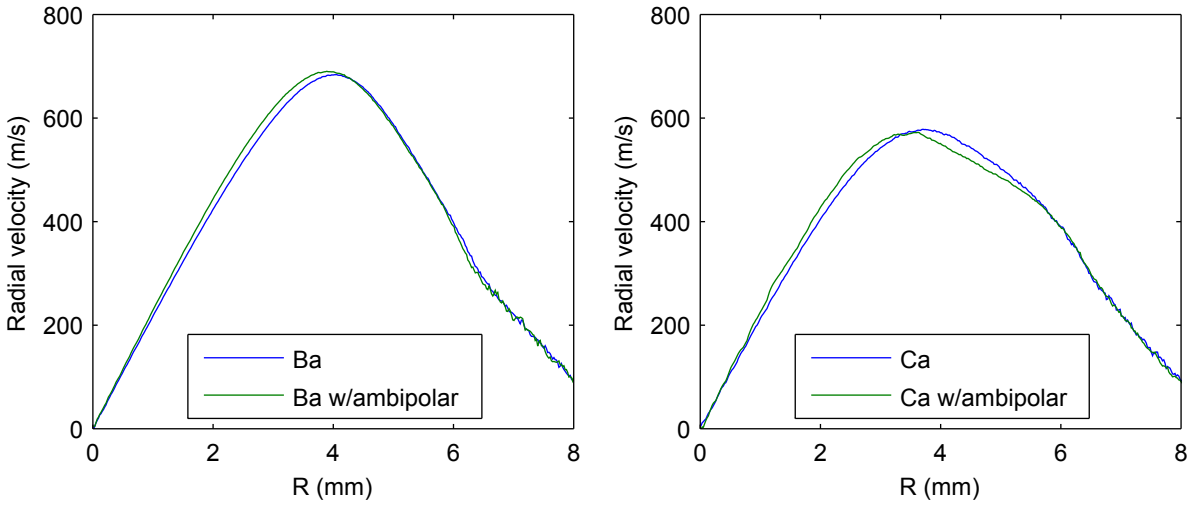

(a) **(b)**

Figure 3.4 The radial velocities for barium (Fig. a) and calcium (Fig. b) 10 mm downstream from the sampling cone.

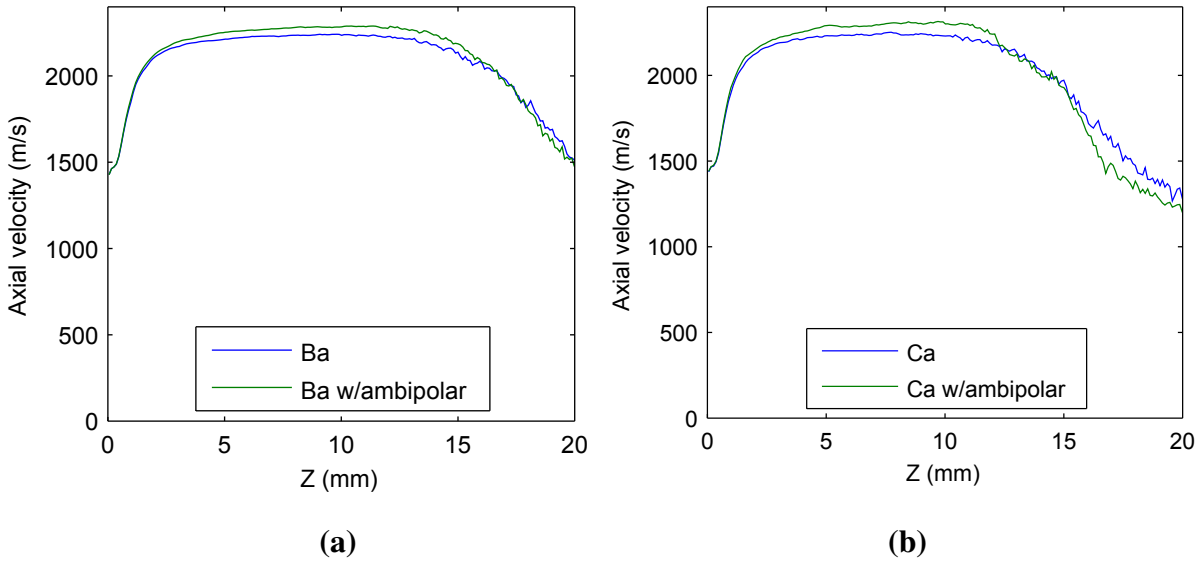

(a) **(b)**

Figure 3.5 Axial velocities for barium (Fig. a) and calcium (Fig. b) on axis.

for the plots with and without ambipolar electric fields are significantly smaller than those seen in the calcium profiles. (Fig. 3.8) Barium has 3.5 times more mass than calcium, therefore the effects of the ambipolar field on barium should be smaller than those on calcium.

As the ICP-MS runs, the sampling cone tip can drift up to 1 mm further upstream due to thermal expansion. Therefore, the uncertainty in the axial position of any experimental data is about 1 mm. To see if the changes to the radial density distributions due to ambipolar field effects are large enough to resolve experimentally, a radial density distribution is taken for both calcium and barium without the ambipolar field. Then, these distributions are compared to the ambipolar radial densities at different axial positions until the radial density distributions for the cases with and without the ambipolar fields match. (See Fig. 3.9) The barium profiles agreed with a 0.2 mm shift in the axial position. The calcium profiles agreed with a 0.4 mm shift in position. Both of these are smaller than the $\sim$1 mm uncertainty in the experimental axial position, therefore it is not feasible to resolve ambipolar field effects in the first vacuum stage with experimental radial density profiles.

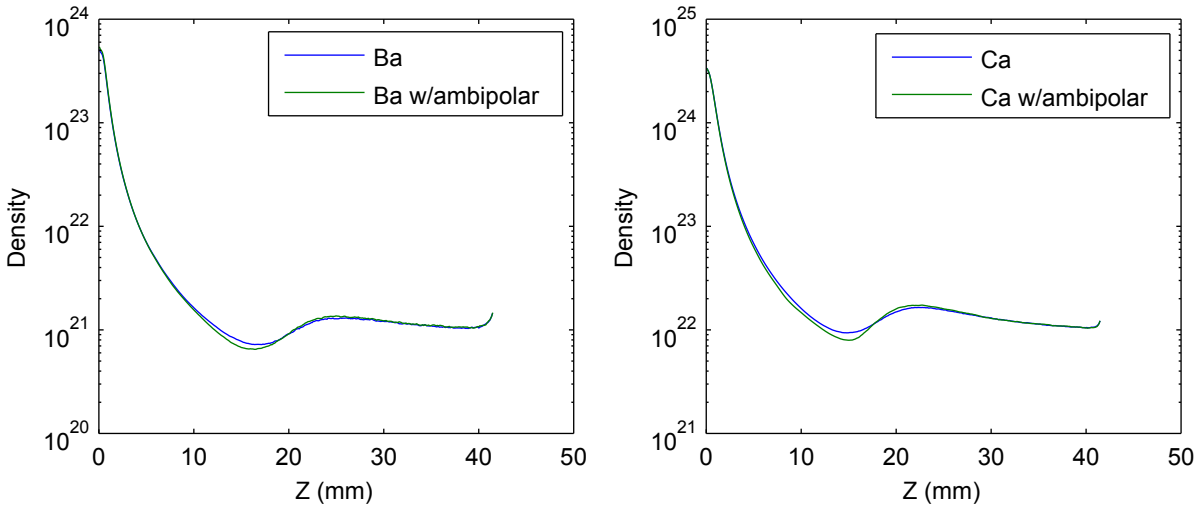

(a) **(b)**

Figure 3.6 Analyte densities along the centerline of the expansion. The plotted densities are in arbitrary units, but they preserve the actual relative densities. The absolute densities are unknown.

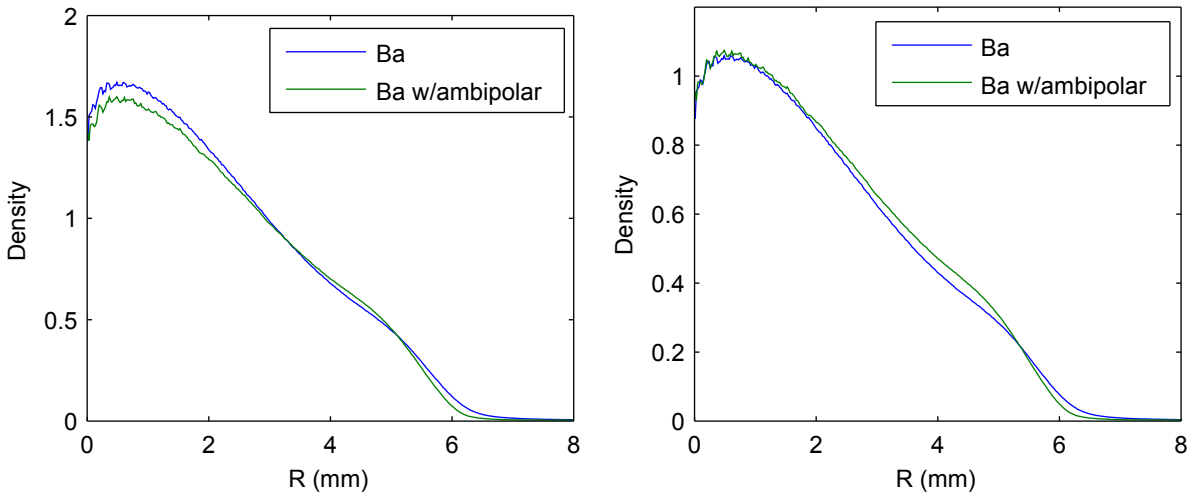

(a) **(b)**

Figure 3.7 Radial density profiles for barium 10 mm behind the sampling cone. Plot (a) shows the relative densities. For plot (b) each density is normalized to its central value.

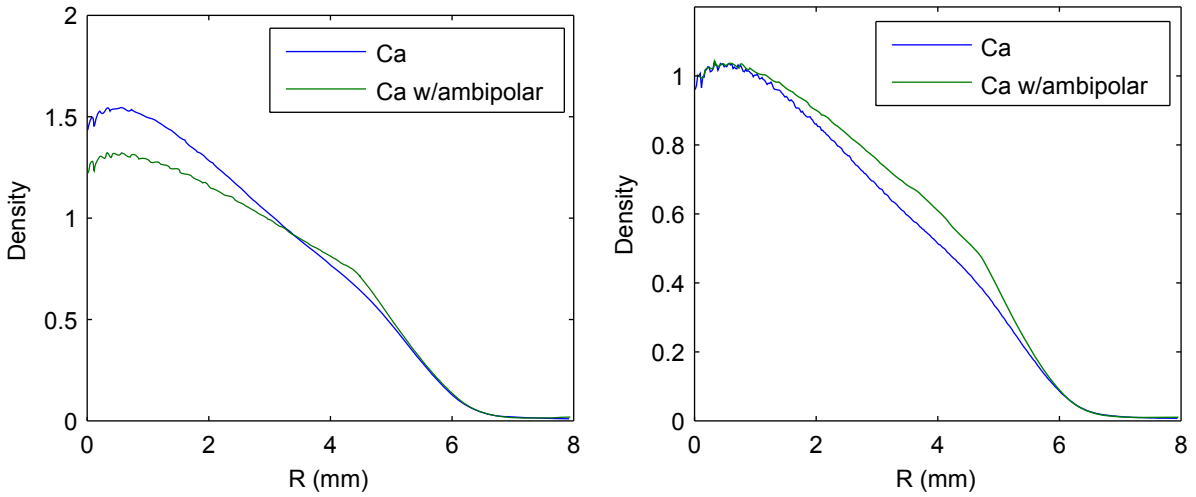

(a) **(b)**

Figure 3.8 Radial density profiles for calcium 10 mm behind the sampling cone. Plot (a) shows the relative densities. For plot (b) each density is normalized to its central value.

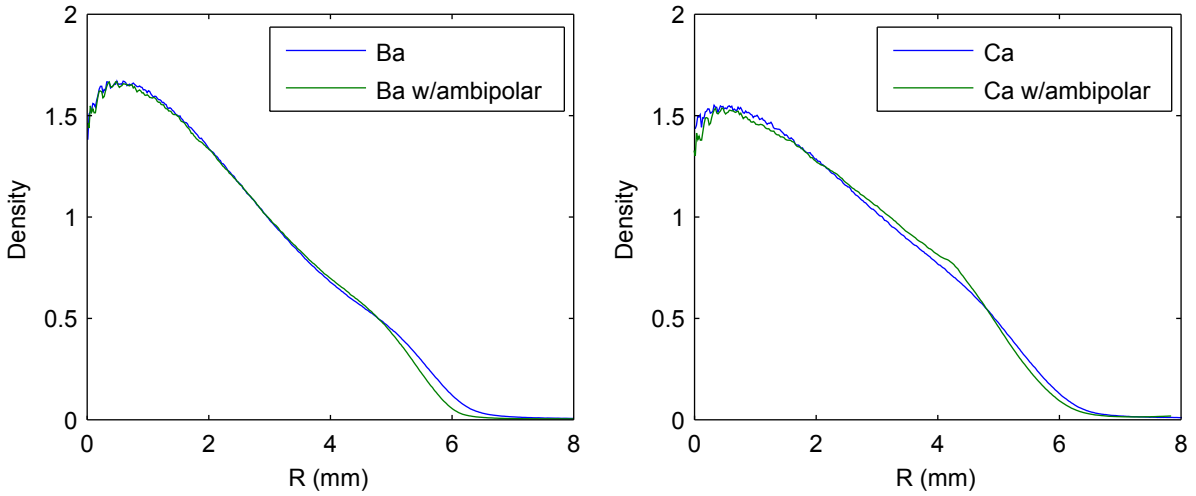

(a) **(b)**

Figure 3.9 Analyte radial densities at 10 mm without ambipolar fields compared to ambipolar fields shifted to a different position so that they match the no field densities. Plot (a) shows barium, and the ambipolar density is from 0.2 mm further upstream. Plot (b) shows calcium, and the ambipolar density is from 0.4 mm further upstream. These profiles have not been normalized in any way.

3.4 Conclusion

Ambipolar fields noticeably affect the analyte behavior in the first vacuum stage of the ICP-MS, especially the axial velocity profiles (3%) and axial density profiles (10%-20%). The differences in axial densities and radial velocities are small enough that they would be very difficult to resolve experimentally. Due to uncertainties caused by the thermal expansion of the skimmer cone, it is also not feasible to resolve ambipolar field effects using radial density profiles. However, the ambipolar field effects can be measured using the analyte axial velocities. [3]

Chapter 4

Plasma Sheaths

4.1 Introduction

When a plasma comes into contact with a conducting surface, the electrons from the plasma are absorbed by the wall. Since the electrons are much more mobile than the ions, a charge imbalance occurs. The ions, now in a positively charged region, are accelerated into the wall by the electric field that has formed and points into the wall. The same field slows the flow of electrons to the surface. Once the ions contact the wall they recombine into neutrals. When this process reaches a steady state, electron and ion fluxes to the wall are roughly equal. (An imbalance creates a secondary discharge.) The ion rich region where the localized electric field forms is called a plasma sheath. [30](See Fig. 4.1) Debye shielding screens the inside of the plasma, so away from the sheath in the bulk of the plasma, the only effect the plasma sees is a slight increase in the plasma potential, which does not affect the overall flow. Note that a large increase in the plasma potential can result in a secondary discharge behind the sampling cone.

As the ions pass into the sheath region, they accelerate to the ion sound speed and beyond. Sheridan and Goree [31] developed a collisional plasma sheath model, that we have been able to

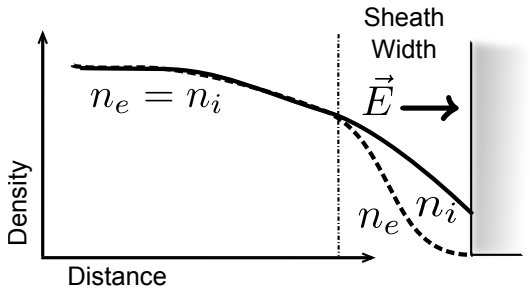

Figure 4.1 Plasma sheath forming against a conducting wall.

adapt to use in conjunction with FENIX.

4.2 Theory

Plasma sheaths are a few Debye (see Eq. 4.5) lengths in size. In the sampling cone of the ICP-MS, the Debye length is about 0.1μm in the bulk of the plasma. To simulate the full sheath using FENIX, the resolution would have to be a fraction of the Debye length, which would make the simulation too computationally expensive to run. Instead, the FENIX data is used in conjunction with the collisional sheath model of Sheridan and Goree. [31]

4.2.1 Collisional Sheath Model

Sheridan and Goree developed a one dimensional, steady state, collisional plasma sheath model. They assume that the electrons are thermal so they obey the Boltzmann relation,

$$n_e = n_0 e^{e\phi/kT_e} \tag{4.1}$$

where n_e is the electron density, n_0 is an initial ion and electron density where the ion and electron densities are still equal, e is the elementary charge, ϕ is the electric potential, k is Boltzmann's constant, and T_e is the electron temperature. In what follows we will use a coordinate system in which x measures the distance perpendicular to the wall.

They continue by including the ion inertia equation:

$$M_i v v' = eE - F_c \tag{4.2}$$

where M_i is the ion mass, v and v' are the ion fluid velocity and its derivative with respect to x, respectively. $\mathbf{F}_c$ is a collisional drag force between argon ions and neutrals. In their paper, Sheridan and Goree calculate the drag force based on the number density and the momentum cross section. Using ion mobility (μ), the collisional term becomes simply $F_c = ev/\mu$. For our calculations, we use the argon ion in argon neutral mobility recorded by Ellis et al. [20–23]. Sheridan and Goree also include the ion continuity equation:

$$n_i v = n_0 v_0 \tag{4.3}$$

where n_i is the ion density, and v_0 is the ion velocity where $n_i = n_0$; and Poisson's equation:

$$\phi'' = -\frac{e}{\varepsilon_0}(n_i - n_e) \tag{4.4}$$

To solve these equations, we scale them according to

$$\eta = \frac{-e\phi}{kT_e} \qquad u = \frac{v}{c_s} \qquad \xi = \frac{x}{\lambda_D} \tag{4.5}$$

where x is a position coordinate measured perpendicular to the wall, c_s is the ion sound speed, and λ_D is the Debye length. The quantities c_s and λ_D are given by:

$$c_s = \sqrt{\frac{kT_e}{M_i}} \quad \lambda_D = \sqrt{\frac{\varepsilon_0 kT_e}{n_0 e^2}} \tag{4.6}$$

The resulting scaled equations are for ion momentum:

$$uu' = \eta' - \alpha u \tag{4.7}$$

where

$$\alpha = \frac{e}{\mu M_i}\frac{\lambda_D}{c_s} \tag{4.8}$$

and Poisson's equation:

$$\eta'' = \frac{u_0}{u} - f e^{-\eta} \tag{4.9}$$

with $f = n_e/n_i$ at $\eta = 0$, where the sheath calculation begins. (See Fig. 4.6 and Sec. 4.2.2) The sheath calculation begins at a carefully chosen point where ambipolar flow in the bulk plasma matches sheath conditions.

4.2.2 FENIX

To simulate a sheath, argon ions were added to the FENIX simulation by fitting the collision integral data of Ellis et al. [20–23] for argon ions in neutral argon to a modified version of Eq. 2.6:

$$\Omega^{(1,1)}(T) = \frac{A\Gamma(3-\nu_1)}{1+\alpha}\left(\frac{m_r}{2k_B}\right)^{\nu_1} T^{-\nu_1} + \frac{B\Gamma(3-\nu_2)}{1+\alpha}\left(\frac{m_r}{2k_B}\right)^{\nu_2} T^{-\nu_2} \tag{4.10}$$

where m_r is the reduced mass, k_B is Boltzmann's constant, and $\alpha = 1.66$. A, B, ν_1, and ν_2 are fitting parameters. The equation was modified to better fit the high temperature behavior of the argon ion in neutral argon collision integral. Eq. 4.10 corresponds to a collisional cross section of

$$\sigma(\theta) = \alpha\left(\frac{A v_r^{-2\nu_1}}{4\pi} + \frac{B v_r^{-2\nu_2}}{4\pi}\right)\left[\cos^2(\theta/2)\right]^{\alpha-1}, \tag{4.11}$$

where v_r is the relative velocity and θ is the center of mass scattering angle. For argon ions, $A = 1.84\times10^{-17}$, $B = 1.10\times10^{-30}$, $\nu_1 = 0.162$, and $\nu_2 = -1.57$. A and B are in S.I. units so that the collision integral of Eq. 4.10 is in m^2.

FENIX's boundary conditions were changed so that whenever a charged particle comes into contact with the sampling cone, it is removed from the simulation. This models the behavior of ions recombining when they come into contact with a conducting wall.

Simply removing the particles from the simulation is not sufficient to form a sheath because the ions undergo significant acceleration due to the sheath's electric field. The electric field can be calculated and added to FENIX using the ambipolar field of Eq. 3.3 as long as the ion and electron densities are approximately equal.

FENIX has too much statistical noise to calculate the ambipolar field in real time. Therefore, the ambipolar field is formed through an iterative process. A FENIX simulation is run, and after it has converged and run long enough to get good statistics, an ambipolar field is calculated from the current results. The calculated field is loaded into FENIX, and the FENIX simulation is started again. This process is then repeated until the ambipolar field converges, and takes about three weeks when running on 100 processors in parallel. Once the ambipolar fields have converged, an algorithm runs around the sampling orifice and loads the ambipolar field, the ion flow speed, the ion density, and the ratio of the electron density to the ion density at a selected distance from the sampling cone wall as initial conditions for the collisional sheath equations. The sheath equations are then numerically solved to calculate the sheath.

To find the best starting point for the sheath solver, starting positions were chosen at varying distances from the sampling cone wall at several different locations around the sampling cone. It was found that as long as $n_e/n_i > 0.98$ and the ion density at the starting position was less than 20% of the central ion density, the resulting electric fields and electron and ion densities varied by less than 10%. Inside the sampling orifice, the sheath solver starting distance was chosen to be 0.02 mm away from the sampling cone wall.

After one simulation was run to convergence for comparison, a much faster iterative process was found that greatly reduced the number of iterations. First, FENIX is run with no ambipolar field, but the ions are still removed from the simulation when they contact the wall. When that simulation finishes, the ambipolar fields are calculated. Then, the sheath solver is run at a few places inside the sampling orifice. The ion flow speeds are too low to form a sheath at this step. To correct for this, we allow the electric potential to be discontinuous at the sheath solver starting point as long as the electron and ion densities are continuous. The next step is to raise the ambipolar fields to the 3/2 power, and then scale their magnitude so that they match the magnitude of the electric field at the points where the sheath was calculated. 3/2 is used because it fits the converged

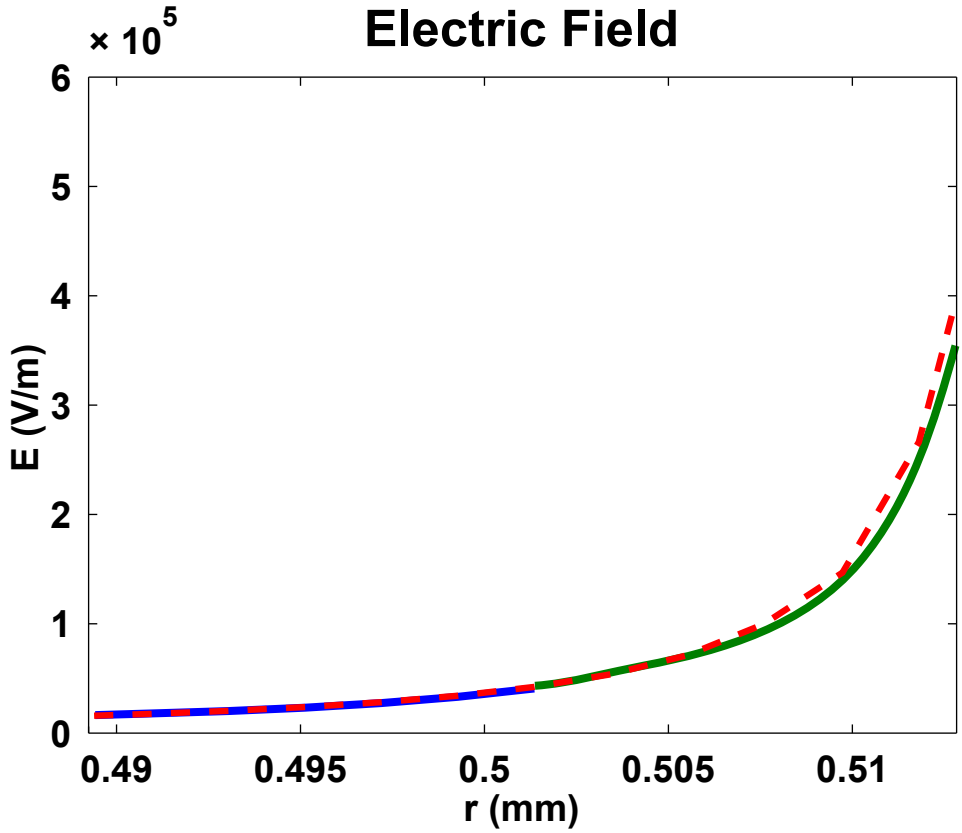

Figure 4.2 Converged electric field solution compared to the scaled ambipolar field approximation. The dashed line shows the approximation. The blue line is the converged electric field from FENIX and the green line is the electric field calculated by the sheath solver.

ambipolar field well. The scaled ambipolar fields are then loaded into FENIX and it is run a second time, and it was found that it gave the same results as when it was allowed to slowly converge. Fig. 4.2 has a plot of the scaled ambipolar field vs. the field that was allowed to converge.

4.3 Results

The plasma sheath around the sampling orifice is too thin to get reliable experimental data to compare it to. However, integrating the resulting electric field (see Fig. 4.3) results in a plasma

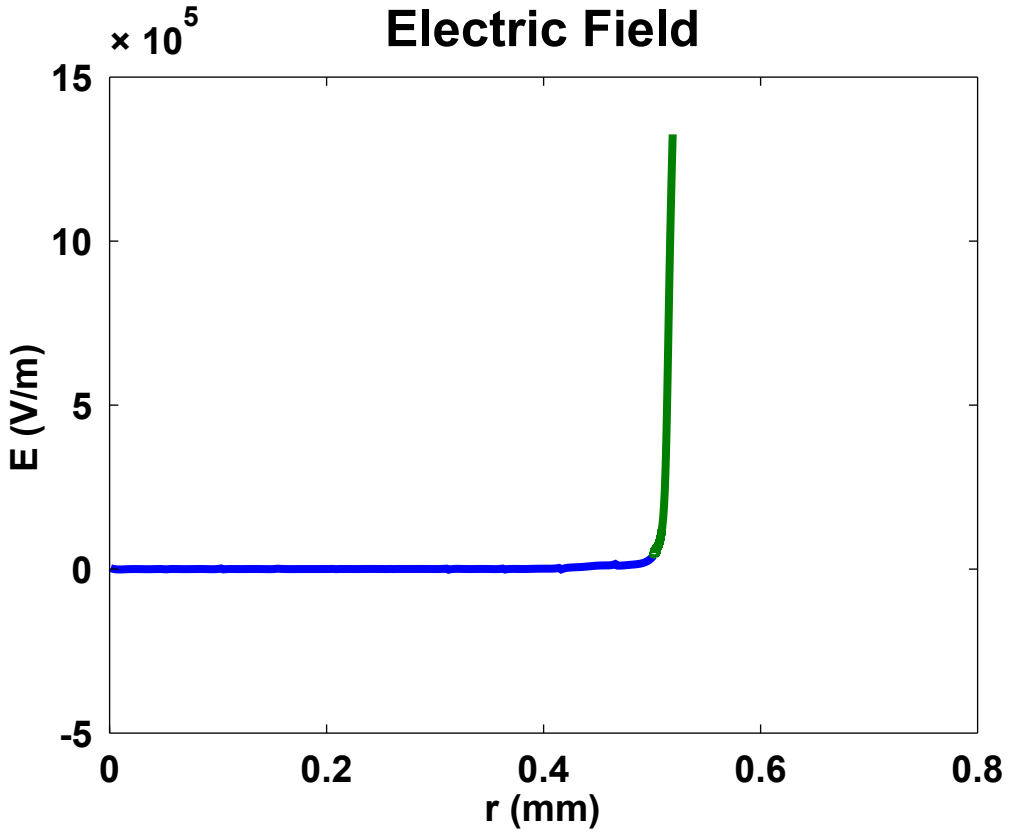

Figure 4.3 Radial plot of the electric field formed by the sheath in the center of the sampling orifice. The blue line is the result from FENIX. The green line was calculated by the sheath solver.

potential of about 7 V, which is comparable to what has been measured experimentally [32].

Figs. 4.4, 4.5, and 4.6 show the resulting electron and ion densities from simulating the sheath. The resulting sheath is about 10 μm wide, only 1/50 of the sampler radius. (See Fig. 4.6) Inside the sheath, the Debye length is 1-2 μm.

The sheath does not affect ion densities inside of a 0.4 mm radius in the sampler, nor is there a significant electric field. (See Figs. 4.3 and 4.7) Therefore, the central plasma is unaffected and once it expands, any effects from the sampler sheath will be at a much larger radius than the skimmer orifice and will not affect the conditions beyond the skimmer.

The sampler sheath does produce one important effect, however: it insulates the electrons from

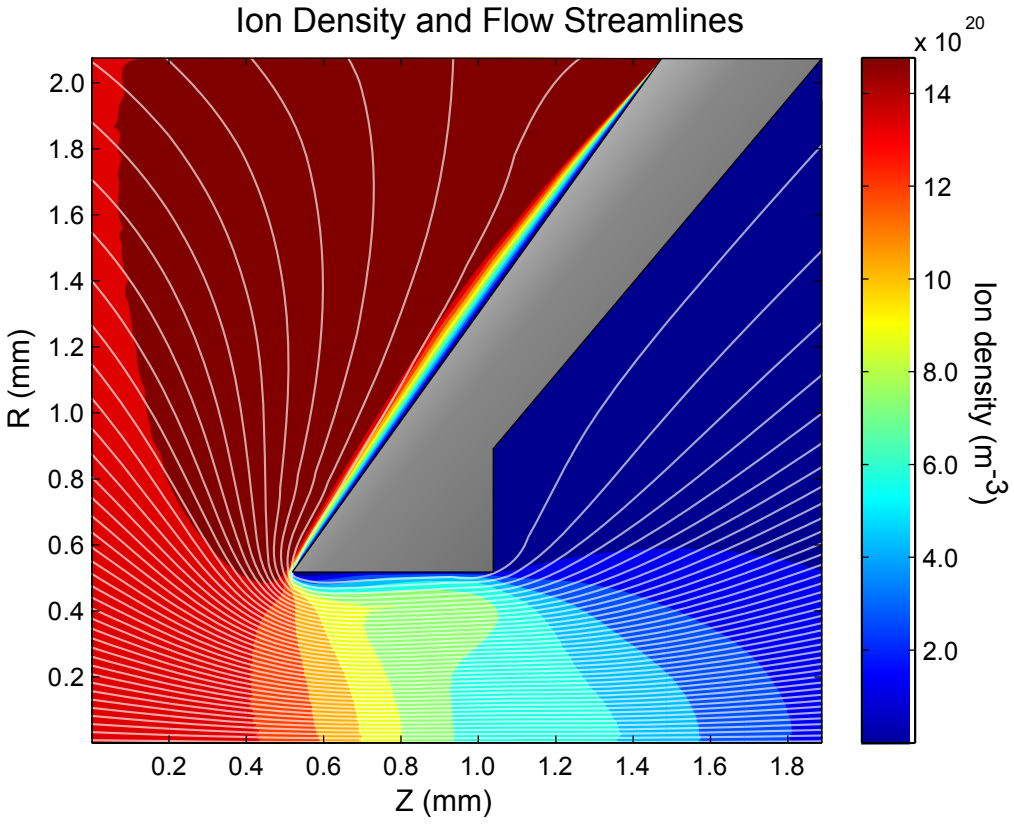

Figure 4.4 Argon ion density overlaid with the streamlines of the flow.

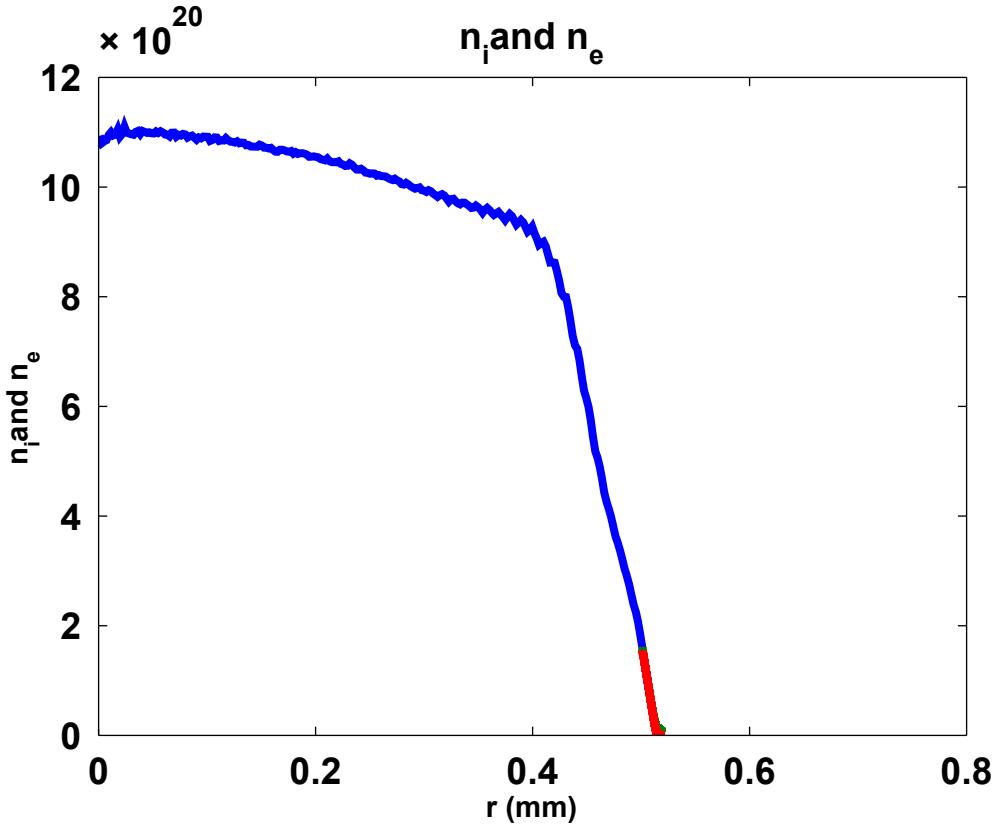

Figure 4.5 Radial plot of the electron/ion density halfway through the sampling orifice. The blue line is the ion density calculated by FENIX. The green line is the ion density calculated by the sheath solver. The red line is the electron density calculated by the sheath solver.

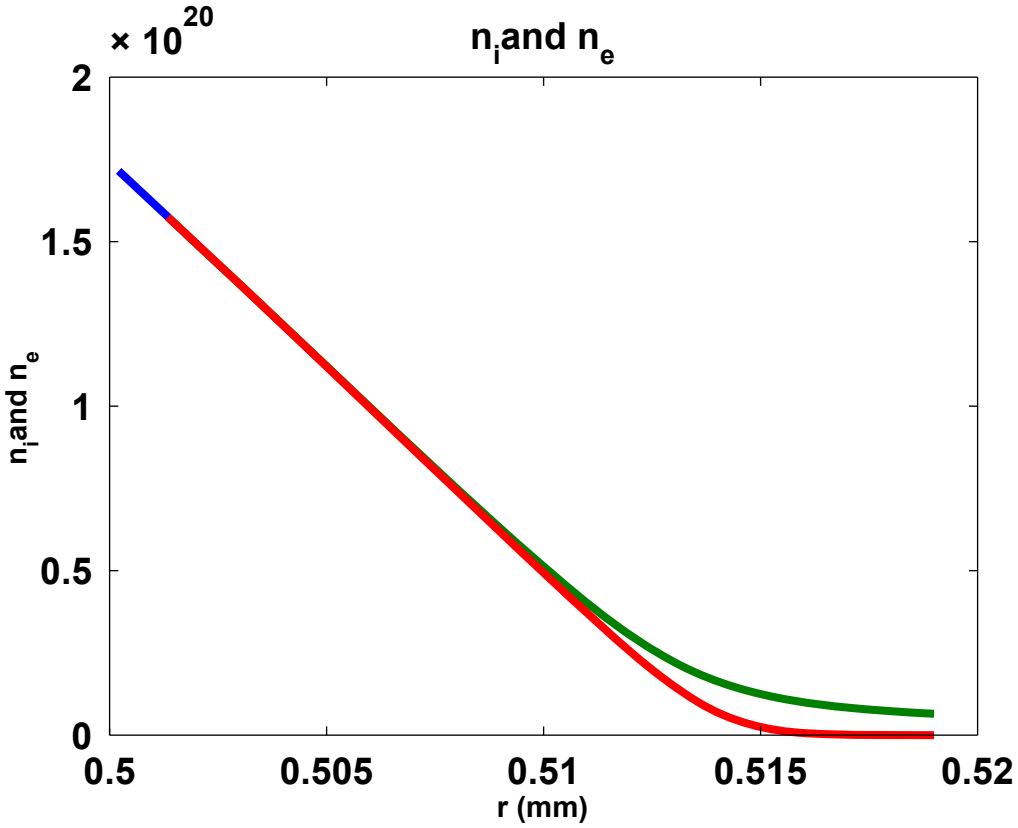

Figure 4.6 Radial plot of the electron/ion density halfway through the sampling orifice, enlarged to show the difference in electron and ion densities near the sampler surface. The blue line is the ion density calculated by FENIX. The green line is the ion density calculated by the sheath solver. The red line is the electron density calculated by the sheath solver. At the point were the blue line meets the green, $\eta = 0$.

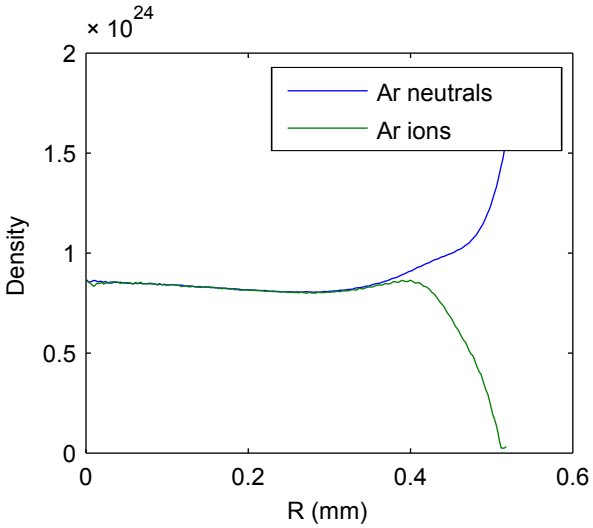

Figure 4.7 Plot of the argon neutral and ion densities. The argon ion densities are 1000 times smaller than plotted. They have been scaled to show their on axis agreement with the argon neutral density.

having thermal contact with the cold sampler surface. Since there are almost no electrons that contact the wall, they lose very little heat to it. The electron thermal conduction coefficient is very high. Fig. 4.8 shows an approximation to what the electron temperature would be if the electrons were in thermal contact with the wall. It was calculated by numerically solving the heat equation:

$$v_z \frac{\partial T}{\partial z} = -\kappa \frac{1}{r} \frac{\partial}{\partial r} \left(r \frac{\partial T}{\partial r} \right) \tag{4.12}$$

where T is the electron temperature, κ is the electron thermal diffusivity, and v_z is the axial flow velocity. For this calculation, v_z is the axial argon flow velocity calculated by FENIX along the axial centerline. Eq. 4.12 was solved numerically on a grid using Crank-Nicolson to advance in z. In less than 1/10 of the way through the sampler, the electrons would be at the temperature of the sampler, several thousand Kelvin colder than what they have been measured to be [33]. In those conditions somewhere between 90% - 99% of the analyte ions would recombine and the ion signal would be lost.

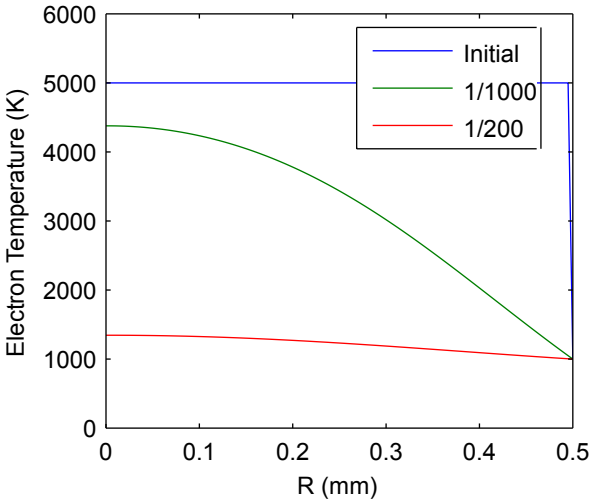

Figure 4.8 Plot of what the electron temperature would be if there were no sheath at the beginning of the sampler, 1/1000 of the way into the sampler, and 1/200 of the way into the sampler.

4.4 Conclusions

FENIX has been used to simulate the plasma sheath that forms around the sampling orifice. The sheath is too narrow to significantly affect the flow through the skimmer and onwards into the detector. It does raise the plasma potential a few volts, which agrees with experimental observations.

The sheath does effectively insulate the electrons from the cold sampler wall. If the electrons were not insulated, they would cool very rapidly and most of the analyte would recombine before it could be detected.

This sheath model has also led to a sheath simulation of the flow behind the skimmer. Early work has shown that sheaths are very important to the charge separation and ion beam formation processes, but that work is beyond the scope of this thesis.

Chapter 5

Simulating Electron/Ion Recombination

5.1 Introduction

Paramount to the performance of the inductively coupled plasma mass spectrometer (ICP-MS) is the efficient transport of analyte ions from the plasma, where they are made, to the mass analyzer. The first step in this process is the free jet expansion of the plasma through the sampling orifice into the first vacuum stage. Due to the expansion, the plasma quickly cools and the density drops by a few orders of magnitude. The cooling plasma encourages electrons and ions to recombine. However, the sharp density drop inhibits electron-ion recombination because the electrons and ions are further apart and less likely to interact.

Douglas and French [1] argued that the density drops so rapidly in the expansion that there is little to no ion-electron recombination, citing the experiments of Fraser et al. [34], who observed that the ion and neutral number densities decayed at about the same rate. However, several later experiments detected evidence of collisional processes affecting the plasma composition after entering the sampling orifice. [35–39]

One set of experiments that offer particular insight into ion-electron recombination in the first

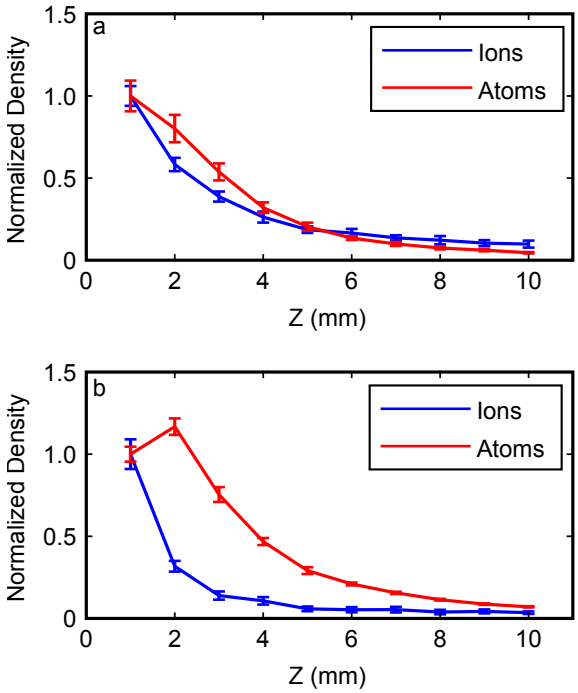

Figure 5.1 Macedone's [17] normalized data. Graph (a) shows the normalized ion and atom signals collected by Macedone at 1100W. Graph (b) shows the normalized ion and atom signals collected at 700 W.

vacuum stage was that of Macedone and Farnsworth. [17] They recorded calcium ion and atom densities at several locations along the axis of the expansion into the first vacuum stage. They showed that the atom and ion densities in the expansion do not have the same shape (see Fig. 5.1) and therefore ions must be recombining into neutrals in the first vacuum stage.

In this dissertation, we compare the results of Macedone and Farnsworth to the output of the direct simulation Monte Carlo algorithm, FENIX. The details of how FENIX simulates the free jet expansion behind the sampling orifice are given in Chapter 2. Through this comparison, we are able to find the ratio of Macedone's and Farnsworth's atom to ion densities as well as the approximate electron-ion recombination rate for each power level in the experiment, the regions where electron-ion recombination is significant, and approximate electron temperatures and densities in the first

vacuum stage.

5.2 Analyzing Macedone and Farnworth's data

Macedone and Farnsworth's experimental data and collection techniques are described in detail in their paper. [17] To summarize, they collected calcium atom and ion densities downstream from the sampling cone for incident powers of both 700 W and 1100 W. The data were collected along the centerline of the expansion in 1 mm increments. They collected the data using laser-induced fluorescence, in a setup where the excitation laser and the collection optics intersected at a 45° angle. The intersection of the excitation laser and the collection optics defined a probe volume. The signal measured at each position correlates to the average density over the probe volume. This gave them a radial resolution of about 1 mm. Near the sampling orifice, the radial density profiles have radii smaller than 1 mm, therefore their apparent density from the fluorescence signal near the sampling cone is smaller than the peak density on the centerline. By 3-4 mm downstream from the sampling cone the density distributions are wide enough that the signal density should correlate to the physical on-axis density. (See Fig. 5.2)

5.2.1 Removing experimental background

Macedone and Farnsworth measured their experimental background by running the ICP-MS with a blank water solution then and subtracting the measured blank signal as a background from their atom and ion measurements. We check for additional background effects by comparing the atom and ion signals to each other as well as to the results of a FENIX simulation for calcium analyte flow in the region. By 4 mm downstream the electron density is low enough that no ion-electron recombination should be occurring. Also, the density distributions should be wide enough that there are no scaling effects from the size of the probe volume. Therefore, the ratio of the atom to

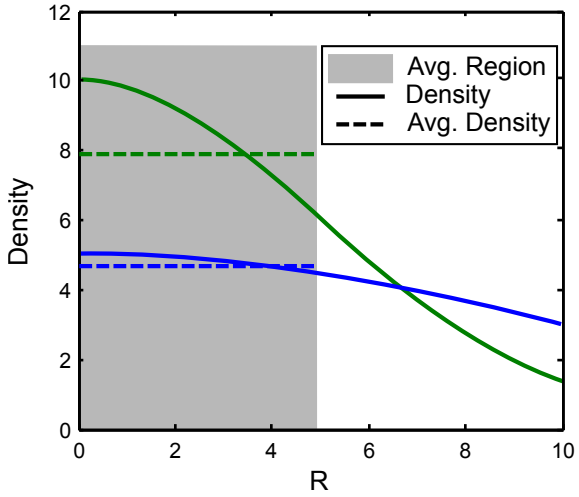

Figure 5.2 Radial plot of two Gaussian density distributions (solid). The dashed lines show the result of averaging each density distribution over the gray area labeled "Avg. Region" assuming cylindrical symmetry about R=0. Notice that for the narrower green distribution, the average density is much lower than the on-axis density. However, the difference is much smaller between the average and on-axis densities for the wider density distribution.

ion densities or to the simulated FENIX calcium density should approach a constant by 4 mm. (See Fig. 5.3) However, the ratio of ion density to atom density as measured in the experiment grows as Z gets large. This implies that the ions have a remaining background signal. When compared to FENIX, both of the atom signals divided by the FENIX produced calcium density approach a constant, whereas both ion signals, when divided by the FENIX produced calcium density continue to increase beyond 4 mm. Therefore, any additional experimental background signal in the atom signals is negligible, but the ions appear to have an additional background. We found the ion signal background by least squares fitting the ion signals from 3 mm to 10 mm to

$$n_I = a(n_f + b) \tag{5.1}$$

where n_f is the on-axis calcium density produced by FENIX, a and b are the fitting parameters, and n_I is the ion signal. For comparison, we also least squares fit the ion density to

$$n_I = a(n_A + b) \tag{5.2}$$

where n_A is the atom density and a and b are fitting parameters. The fit to Eq. 5.2 was started at 4 mm downstream from the sampling cone. We found that the 700 W ion signal needed an additional 0.04 V (3% of the signal peak) removed as background and the 1100W needed 0.15 V (7 % of the signal peak) removed. The calculated background signals are only a few percent of the peak ion signal. It is unknown why only the ions needed to be adjusted for additional background signal. Fig. 5.4 shows the good agreement in the large Z behavior of atoms and ions once the additional ion background has been removed.

5.2.2 Conservation of Mass

Macedone's and Farnsworth's ion and atom signals should relate to the actual on-axis number density through:

$$n_{axis} = SG(z)N_s \tag{5.3}$$

where N_s is the experimentally measured ion or atom signal; n_{axis} is the physical atom or ion density on axis; S is the constant that converts the experimental signal to a physical density; $G(z)$ is a scaling function that converts the experimental signal into an on-axis density with $G(z) = 1$ at large z. Both ion measurements should have the same S value (S_I), as should both of the atom measurements (S_A), since S depends on how the ions and atoms interact differently with their excitation lasers.

Macedone and Farnsworth tried to keep all of the flow parameters the same between the 700 W and 1100 W experiments except for the incident power. However, some of the calcium might still have been trapped in unvaporized droplets, especially in the colder 700 W torch. Applying

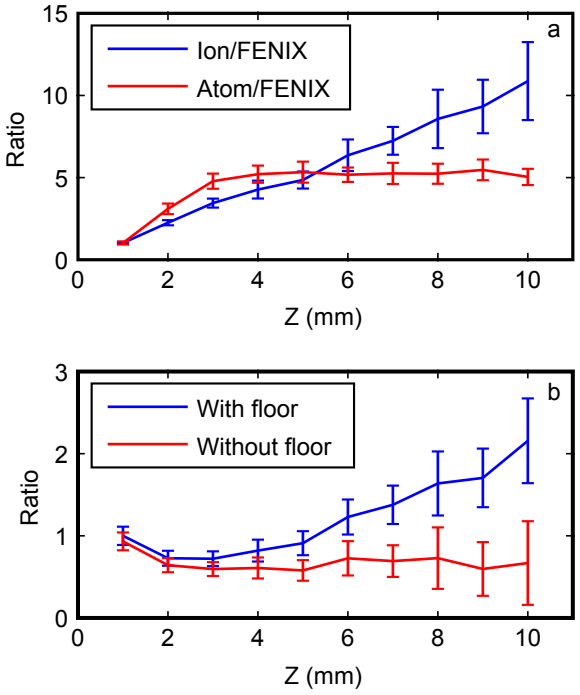

Figure 5.3 Graph (a) shows Macedone's normalized ion and atom signals at 1100 W divided by the on-axis calcium density produced by FENIX. Graph (b) shows the ratio of Macedone's normalized ion signal to his normalized atom signal at 1100 W. With floor shows the ratio of the unaltered data. Without floor shows the ratio with the ion background signal removed. Notice that once the ion background is removed, the ratio of the ion to atom signals in graph(a) is roughly flat beyond Z=2-3 mm. The error bars were calculated using Gaussian error propagation on the experimental error.

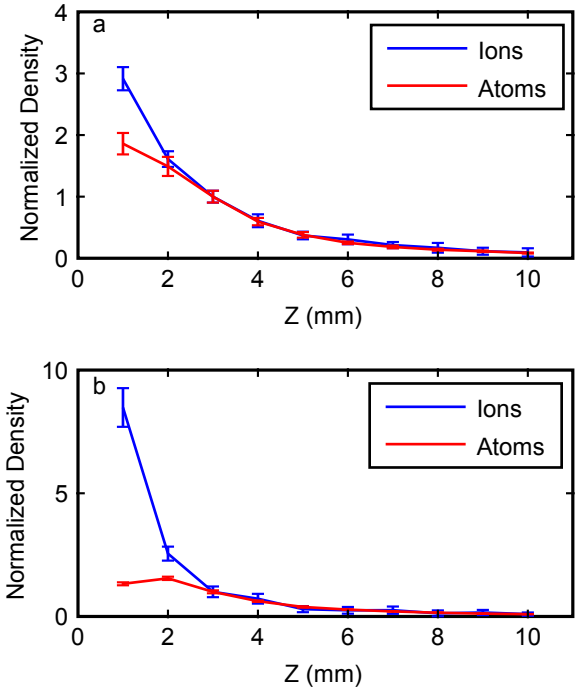

Figure 5.4 Plots of Macedone's data with the ion signal background removed. Graph (a) shows the atom and ion densities for 1100 W of incident power. Graph (b) shows the atom and ion densities for 700 W of incident power. The densities have been normalized to their values at 3 mm downstream from the sampling cone in order to emphasize the good agreement in their downstream behavior.

that fact to conservation of mass gives:

$$C\left(n_A^{1100}+n_I^{1100}\right)=n_A^{700}+n_I^{700} \tag{5.4}$$

where n is a physical density, n_A is the actual atom density, and n_I is the actual ion density. The superscripts denote the incident power. C is a constant that scales between the two incident powers to account for differences in the total amount of calcium due to having some of the calcium trapped in droplets. Using Eq. 5.3 to convert the physical densities of 5.4 into signal densities, canceling out the factor $G(z)$ in each term, and dividing by S_I:

$$C\left(\frac{S_A}{S_I}N_A^{1100}+N_I^{1100}\right)=\frac{S_A}{S_I}N_A^{700}+N_I^{700} \tag{5.5}$$

where N is the experimentally measured signal. Least squares fitting Eq. 5.5 to Macedone's and Farnsworth's data gives $C=0.85$ and $\frac{S_A}{S_I}=0.25$. $C=0.85$ means that the total calcium density at 700 W is 85% of the total calcium density at 1100 W. Fig. [5.5] shows the results of the fit. The good agreement between both sides of Eq. 5.5 supports the assumption that $G(z)$ is the same for both 700 W and 1100 W.

The percentage of calcium that is ionized can be calculated through:

$$\frac{n_I}{n_A+n_I}=\frac{S_I G(z) N_I}{S_A G(z) N_I+S_I G(z) N_I}=\frac{N_I}{S_A/S_I N_A+N_I} \tag{5.6}$$

The calculated ionization percentages are presented in Fig. [5.6]. At 1100 W, the percentage of calcium that is ionized drops from $Z=1$ mm to 2 mm. Beyond 2 mm it is constant within experimental error. Therefore at 1100 W, electron-ion recombination stops by 2 mm downstream from the sampling orifice. At 700 W, the percentage of calcium that is ionized drops until 3 mm downstream. After recombination stops, the ions make up 63% of the total calcium density in the 1100 W case, and only 20% in the 700 W case.

Using the same methods described in their paper, Macedone and Farnsworth collected ion and atom signals just upstream from the sampler tip. [40] They are presented in Table 5.1. Using the

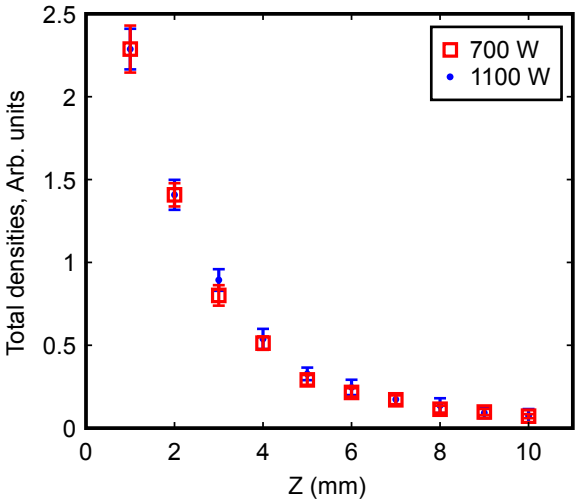

Figure 5.5 The result of least squares fitting to the total calcium density (Eq. 5.5). The error bars were calculated using Gaussian error propagation on the experimental data. These densities have not been scaled by the factor $G(z)$.

	Ion Signal (V)	Atom Signal (V)
700 W	1.00 ± 0.05	0.74 ± 0.09
1100 W	1.85 ± 0.06	0.45 ± 0.08

Table 5.1 Ion and atom signals measured by Macedone and Farnsworth just upstream from the sampling cone. Each data point is the average of 33 replicate measurements with their standard deviation.

values in the table, just upstream from the sampling cone 95% of the calcium is ionized in the 1100 W case and 84% is ionized at 700 W. Using the Saha equation (Eq. 5.22) to calculate the electron temperature and density upstream gives value ranges that are comparable to those measured by Gamez et al. [29] for similar incident powers. Comparing the upstream ionization percentages to the final downstream ones shows that at 1100 W, the ion density drops by a factor of 1.5 while traveling through the sampler. At 700 W, the ion density drops by a factor of 4.2.

Since the FENIX simulation does not include electron-ion recombination, the on-axis calcium

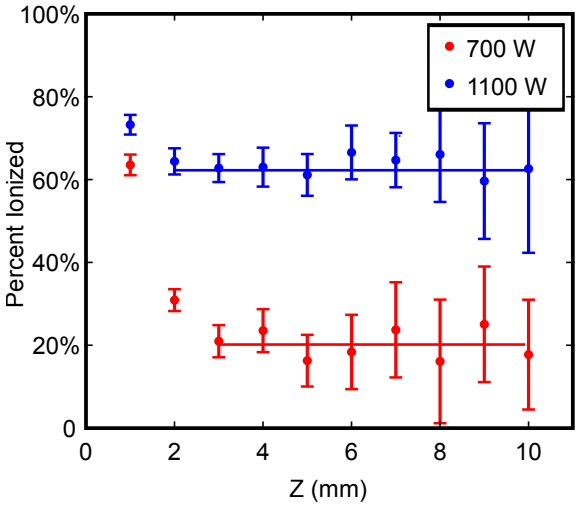

Figure 5.6 The percentage of calcium that is ionized as a function of downstream position. The solid horizontal lines were found by fitting the points that each lines spans to a constant using an error-weighted least squares fit. The error bars were calculated using Gaussian error propagation.

densities produced by FENIX should be proportional to the total density:

$$\frac{S_A}{S_I} N_A G(z) + N_A G(z) = \beta n_f \tag{5.7}$$

where n_f is the on-axis FENIX calcium density, and β is some constant. From this equation, the geometry scaling function $G(z)$ can easily be calculated from either the 700 W or the 1100 W data. Using least squares fitting Eq. 5.7 to both the 700 W and 1100 W data gives

$$G(z) \approx 2.67 \exp\left[-\frac{z - z_0}{6.52e-4}\right] + 1 \tag{5.8}$$

where z is the distance from the sampling cone in meters and $z_0 = 1$ mm. Fig. 5.7 shows the good agreement between the $G(z)$ functions calculated at 700 W, 1100W, and Eq. 5.8. Since β is unknown, $G(z)$ is normalized so that it is unity at large z for convenience in converting the measured ion and atom signals to on-axis densities.

To check if $G(z)$ is reasonable, a program was written that integrates FENIX data interpolated onto a 3-D grid over the collection probe volume of the experiment. Centering the probe volume

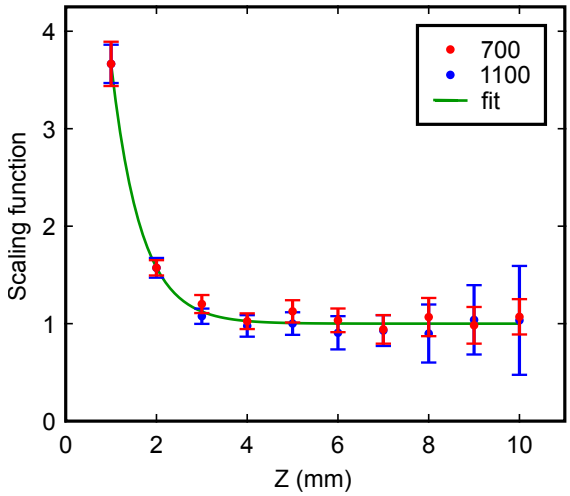

Figure 5.7 Graph showing $G(z)$, the function that scales the experimental data to an on-axis density. 700 shows G calculated from the 700 W data. 1100 shows $G(z)$ calculated from the 1100 W data. Fit is the least squares fit to both the 700 W and 1100 W scaling functions.

along the sampler centerline predicts a $G(z)$ whose value at Z= 1 mm is about half of the $G(z)$ calculated from the experimental data. However, the integration program was able to reproduce the calculated $G(z)$ by having the center of the probe volume sit about 100 μm below the sampler centerline, which is well within experimental error. Also, the testing program only integrated axisymmetric data, so the source of the disagreement between the on-centerline calculated $G(z)$ and the $G(z)$ calculated from the experimental data could also be some asymmetry in the expansion or some unaccounted for flaw in the collection optics. The difference could also be the result of the initial radial calcium density profile loaded into FENIX being wider than the actual radial density distribution. The effect of narrowing FENIX's initial radial calcium density by 20% affected $G(z)$ about the same amount as shifting the center of the probe volume about 10-20 μm.

There are no data that will allow the calcium ion and atom densities to be linked to a physical density. However, using Eq. 5.3 with the calculated S_A/S_I and $G(z)$ allows Macedone's and Farnsworth's data to be plotted as relative densities. (See Fig. 5.8) Note that the apparent increase

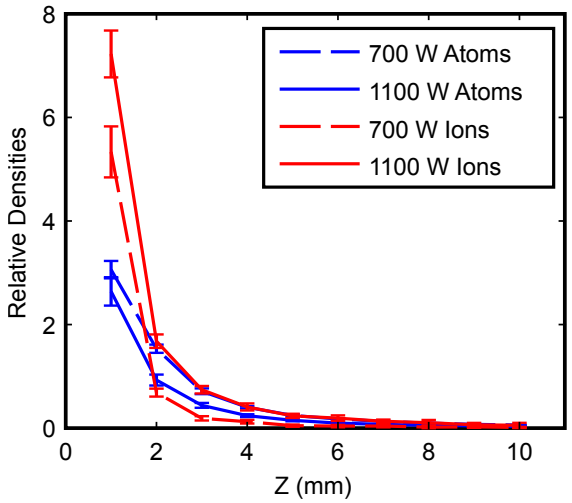

Figure 5.8 Macedone's data converted into on-axis densities using S and G. The absolute calcium density is unknown, but these traces capture the relative densities between the four atom/ion populations.

in the atom density seen by Macedone and Farnsworth from 1-2 mm at 700 W (See Fig. 5.1) is an artifact of their data collection techniques. Once their atom signal at 700 W is converted to an on-axis density, the atom density decreases throughout the expansion. The free jet expansion is still the dominant feature of the on-axis calcium densities.

5.3 Theoretical Model

5.3.1 Relating Ion, Atom, and FENIX densities

With some additional analysis, the electron-ion recombination rate can be estimated from the experimental data and from FENIX. To begin, in Chapter 2, it was shown that FENIX analyte satisfies:

$$n_f \nabla \cdot \mathbf{v} + \mathbf{v} \cdot \nabla n_f = \nabla \cdot \left(D \nabla n_f \right) \tag{5.9}$$

where v is the flow velocity, D is the diffusion coefficient, and n_f is the FENIX analyte density.

The calcium ions in the expansion also follow Eq. 5.9, but with source and sink terms added for ionization and recombination:

$$n_i \nabla \cdot \mathbf{v} + \mathbf{v} \cdot \nabla n_i = \nabla \cdot (D \nabla n_i) - K_r n_i + K_i n_a \tag{5.10}$$

where n_i is the ion density, K_r the electron-ion recombination rate, and K_i is the ionization rate. The calcium atom equation is:

$$n_a \nabla \cdot \mathbf{v} + \mathbf{v} \cdot \nabla n_a = \nabla \cdot (D \nabla n_a) + K_r n_i - K_i n_a \tag{5.11}$$

Using the values calculated in Sec. 5.4.1, in the 700 W case, one millimeter downstream from the sampling cone, K_i is somewhere between $10^4 \sim 10^5$ times smaller than K_r. In the 1100W case, $K_r \approx 10 K_i$, and since there are more ions than atoms, $K_i n_a$ is only about 3% of $K_r n_i$, which is much smaller than the uncertainty in the calculated K_r. Therefore, it is safe to assume that $K_i \approx 0$.

Also, convection dominates over diffusion in the expansion. The changes in density and velocity on-axis due even to ambipolar diffusion are much smaller than the experimental error in Macedone's and Farnsworth's data, therefore, within 5% or so, we may assume that $D \approx 0$ and $v_i \approx v_a$. Also, on-axis there is no radial velocity. Therefore, along the center line $\mathbf{v} \cdot \nabla = |v| \frac{\partial}{\partial z}$. The quantity $\nabla \cdot \mathbf{v}$ is calculated directly from the FENIX-produced calcium ion flow velocity. Based on these assumptions, Eq. 5.9 simplifies to:

$$n_f \nabla \cdot \mathbf{v} + |v| \frac{\partial n_f}{\partial z} = 0 \tag{5.12}$$

which can be rearranged to:

$$\frac{\nabla \cdot \mathbf{v}}{|v|} = -\frac{1}{n_f} \frac{\partial n_f}{\partial z} \tag{5.13}$$

Simplifying and rearranging Eq. 5.10 gives:

$$\frac{1}{n_i} \frac{\partial n_i}{\partial z} + \frac{\nabla \cdot \mathbf{v}}{|v|} = -\frac{K_r}{|v|} \tag{5.14}$$

Substituting in Eq. 5.13 gives:

$$\frac{1}{n_i}\frac{\partial n_i}{\partial z} - \frac{1}{n_f}\frac{\partial n_f}{\partial z} = -\frac{K_r}{|v|} \tag{5.15}$$

Integrating both sides and solving for n_i gives:

$$n_i = \frac{n_{i0}}{n_{f0}} n_f \gamma(z) \tag{5.16}$$

where n_{i0} is the initial ion density, n_{f0} is the initial FENIX density, and

$$\gamma(z) = \exp\left[-\int_{z_0}^{z} \frac{K_r}{|v|} dz\right] \tag{5.17}$$

Since the FENIX calcium density is proportional to the total calcium density, conservation of mass gives:

$$\frac{n_a + n_i}{n_{a0} + n_{i0}} = \frac{n_f}{n_{f0}} \tag{5.18}$$

where n_{a0} is the initial atom density. Substituting in n_i from Eq. 5.16 and solving for n_a gives:

$$n_a = n_f \left[\frac{n_{a0}}{n_{f0}} + \frac{n_{i0}}{n_{f0}}(1 - \gamma(z))\right] \tag{5.19}$$

5.3.2 Calculating Ion Density and Electron Temperature

To find $\gamma(z)$ we need the electron density, n_e, and the electron temperature, T_e. We start with the collisional-radiative recombination rate (K_r) calculated by Stevefelt [41]:

$$\begin{aligned} K_r = 4.26 \times 10^{-19} \frac{1}{T_e^{0.63}} + 4.98 \times 10^{-26} \frac{n_e^{0.37}}{T_e^{2.13}} \\ + 1.94 \times 10^{-39} \frac{n_e}{T_e^{4.5}} \ [m^3/s] \end{aligned} \tag{5.20}$$

where T_e is in eV and n_e is the electron density in units of m^{-3}.

For comparison, the ionization rate (K_i) can be found using detailed balance. In thermal equilibrium:

$$K_i n_n n_e = K_r n_e n_i \tag{5.21}$$

where n_n is the neutral density and n_i is the ion density. Using Saha's equation:

$$\frac{n_i n_e}{n_n} = 2\left(\frac{2\pi m_e k_B T_e}{h^2}\right)^{3/2} \frac{Z_i}{Z_n} e^{-E_\infty/k_B T_e} \tag{5.22}$$

where m_e is the electron mass, k_B is Boltzmann's constant, h is Planck's constant, E_∞ is the ionization energy of the atom, and Z_i and Z_n are the ion and neutral partition functions, respectively. Combining Eq. 5.22 with Eq. 5.21 gives:

$$\begin{aligned} K_i &= \frac{n_i n_e}{n_n}\frac{K_r}{n_e} \\ &= 2\left(\frac{2\pi m_e k_B T_e}{h^2}\right)^{3/2} \frac{Z_i}{Z_n} e^{-E_\infty/k_B T_e}\frac{K_r}{n_e} \end{aligned} \tag{5.23}$$

Both the recombination and ionization rates depend on the electron density and temperature. It would be too computationally expensive to do a full electron simulation with FENIX, so an approximate on-axis electron temperature and density are calculated by first solving the electron density equation:

$$n_e \nabla \cdot \mathbf{v} + \mathbf{v} \cdot \nabla n_e = \sum_l K_l n_l - K_r n_e \tag{5.24}$$

where K_l and n_l are the ionization rates and densities for every species in the plasma. Since the majority of the electrons come from the argon plasma, we assume that only the argon ionization term is significant, giving:

$$n_e \nabla \cdot \mathbf{v} + \mathbf{v} \cdot \nabla n_e = K_{net}(n_e, T_e) n_e \tag{5.25}$$

where

$$K_{net} = (K_{Ar} - K_r) n_e \tag{5.26}$$

and K_{Ar} is the argon ionization rate.

The electron temperature is calculated using the fluid electron energy equation:

$$\mathbf{v} \cdot \nabla T_e + \frac{2}{3} T_e \nabla \cdot \mathbf{v} = \frac{2}{3 n_e} \nabla \cdot (\kappa \nabla T_e) + \frac{2}{3} S \tag{5.27}$$

where $\mathbf{v}$ is the argon flow velocity taken from FENIX, κ is the electron thermal conductivity, and S includes two additional source terms. The first source term describes the thermal equilibration between the electrons and the argon plasma

$$\bar{\nu}_{\varepsilon}^{e|i}(T_{Ar} - T_e) \tag{5.28}$$

where $\bar{\nu}_{\varepsilon}^{e|i}$ is the thermal equilibration coefficient [42] and T_{Ar} is the argon plasma temperature. The second source term is ionization cooling/recombinative heating

$$2K_{net}k_B T_e \tag{5.29}$$

That term includes the effect that for every electron that recombines, it gives about $2kT_e$ of energy to the free electrons [43].

Upstream from the sampling tip, Eqs. 5.25 and 5.27 can be approximated as:

$$n_e \nabla \cdot \mathbf{v} + v_z \frac{dn_e}{dz} = K_{net}(n_e, T_e) n_e + C_n \tag{5.30}$$

and

$$v_z \frac{dT_e}{dz} + \frac{2}{3} T_e \nabla \cdot \mathbf{v} = \frac{2}{3n_e} \frac{d}{dz}\left(\kappa \frac{dT_e}{dz}\right) + \frac{2}{3}\bar{\nu}_{\varepsilon}^{e|i}(T_{Ar} - T_e) + \frac{4}{3}K_{net}k_B T_e + C_T \tag{5.31}$$

where C_n and C_T are constants chosen so that $n_e'(z_0) = 0$ and $T_e'(z_0) = 0$ where $z_0 = -2$ mm (2 mm upstream from the tip of the sampling cone). These constants approximate any contributions from the radial derivatives in Eqs. 5.25 and 5.27, with the exception of the $\nabla \cdot \mathbf{v}$ term. The quantity $\nabla \cdot \mathbf{v}$ is calculated from the two-dimensional argon flow velocity produced by FENIX. Near the sampler tip and through the sampling orifice, the radial terms in Eqs. 5.25 and 5.27 are small compared to the axial terms, so for $Z > -0.1$ mm (0.1 mm upstream from the sampling cone tip) C_n and C_T are set to zero.

Downstream from the sampling cone, the vector derivatives are computed by assuming the electrons expand spherically as calculated by Ashkenas and Sherman [8] where z is the radial

coordinate. This assumption changes Eq. 5.31 to:

$$v_z\frac{dT_e}{dz}+\frac{2}{3}T_e\nabla\cdot\mathbf{v}=\frac{2}{3n_e}\frac{1}{z}\frac{d}{dz}\left(z\kappa\frac{dT_e}{dz}\right)+\frac{2}{3}\bar{\nu}_\varepsilon^{e|i}\left(T_{Ar}-T_e\right)+\frac{4}{3}K_{net}k_BT_e \tag{5.32}$$

These equations are solved iteratively using finite differencing.

Once the electron temperature and density are found, the analyte densities can be found by first substituting the resulting n_e and T_e into Eq. 5.20 to find K_r, then substituting K_r into Eq. 5.17 to find $\gamma(z)$ and finally substituting the calculated $\gamma(z)$ into Eqs. 5.16 and 5.19 to find n_A and n_I.

5.4 Results and Discussion

5.4.1 Calculating K_r from the experiment.

Before proceeding with the calculation described in Sec. 5.3, we note that the recombination rate can be calculated directly from the experimental data by solving Eq. 5.16 for K_r:

$$K_r=|v|\frac{\partial}{\partial z}\ln\left(G(z)\frac{n_{f0}}{n_{i0}}\frac{n_i}{n_f}\right) \tag{5.33}$$

The logarithm can be separated into $\ln\left(n_{f0}/n_{i0}\right)+\ln\left(G(z)n_i/n_f\right)$. The first term is a constant, so its derivative is zero. Therefore all of the normalization factors between n_i and n_f disappear and K_r can be calculated directly from Macedone's data using:

$$K_r=|v|\frac{\partial}{\partial z}\ln\left(G(z)\frac{n_i}{n_f}\right) \tag{5.34}$$

The results of that calculation are presented in Table 5.2. Since the experimental data are discrete, the recombination rates in Table 5.2 are the average values between Macedone's data points.

The rates in Table 5.2 allow for a wide range of electron temperatures and densities. (See Fig. 5.9) However, the range of values can be limited by using the temperature and energy calculations of Sec. 5.3.2. The electron density and temperature equations are solved numerically, taking only

	Avg. recombination rate (s^{-1})		
Incident power	1-2 mm	2-3 mm	3-4 mm
700 W	1.5e+6 $\pm$ 2.8e+5	9.8e+5 $\pm$ 4.9e+5	4.0e+5 $\pm$ 7.0e+5
1100 W	2.6e+05 $\pm$ 2.0e+05	3.5e+04 $\pm$ 2.6e+05	2.2e+04 $\pm$ 4.0e+05

Table 5.2 Recombination rates calculated by combing FENIX with Macedone's data using Eq. 5.34. The error was calculated using Gaussian error propagation. Note that for 1100 W, due to the large error inherent in taking derivatives of experimental data, the rate cannot be determined at 2 mm or beyond. For 700 W, the rate cannot be determined at 3 mm or beyond.

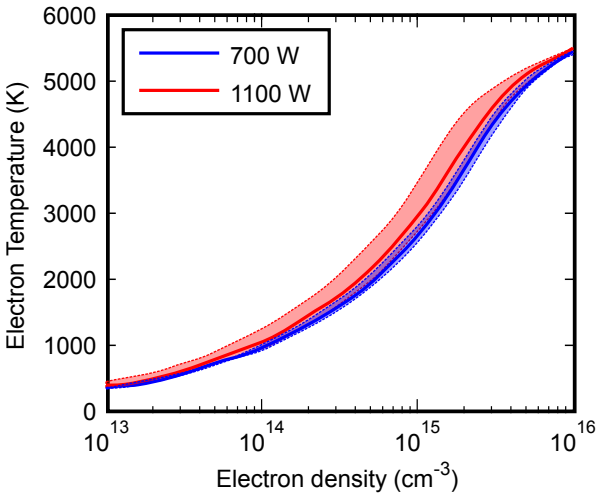

Figure 5.9 The range of possible electron densities and temperatures that will satisfy the 1-2 mm average recombination rates of Table [5.2].

an initial upstream temperature and density as inputs, and then calculating the downstream values. Two parameters were considered to narrow the range of acceptable initial conditions. First, the initial temperature and density had to match the estimated upstream ionization percentage when predicted by the Saha equation to within a few percent. Second, the resulting $\gamma(z)$ had to match not just the values in Table 5.2, but also had to reproduce the geometry-corrected experimental densities when substituted into Eqs. 5.16 and 5.19. Fig. 5.10 shows the calculated on-axis densities vs. the geometry scaled experimental data. Figs. 5.11 and 5.12 show the electron temperatures and densities used to calculate the analyte densities of Fig. 5.10.

Even with the constraints on the calculated electron densities and temperatures, the electron temperature could vary by about 20% and still satisfy the conditions, as long as the initial electron density was scaled accordingly. The electron density could vary as much as 50%.

It is interesting to note the effect of the large electron thermal conduction coefficient. The gas flow rates are high enough through the expansion that the upstream argon has no thermal contact with the cold gas in the expansion. However, the warm upstream electrons are able to conduct heat to the colder downstream electrons keeping them significantly hotter than the rest of the expanding plasma, as has been observed experimentally. [33]

5.4.2 General recombination properties

While Macedone's and Farnsworth's experimental data only allow for a rough calculation of the electron temperatures and densities, they do allow the formation of a clearer picture of electron-ion recombination through the sampling orifice. Fig. 5.13 shows the general behavior of recombination. The figure was produced using the 1100 W electron temperatures and densities from Figs. 5.11 and 5.12.

From about the center of the sampling orifice and further upstream, the ionization rate is comparable to the recombination rate. This couples Eqs. 5.10 and 5.11, making their solutions much

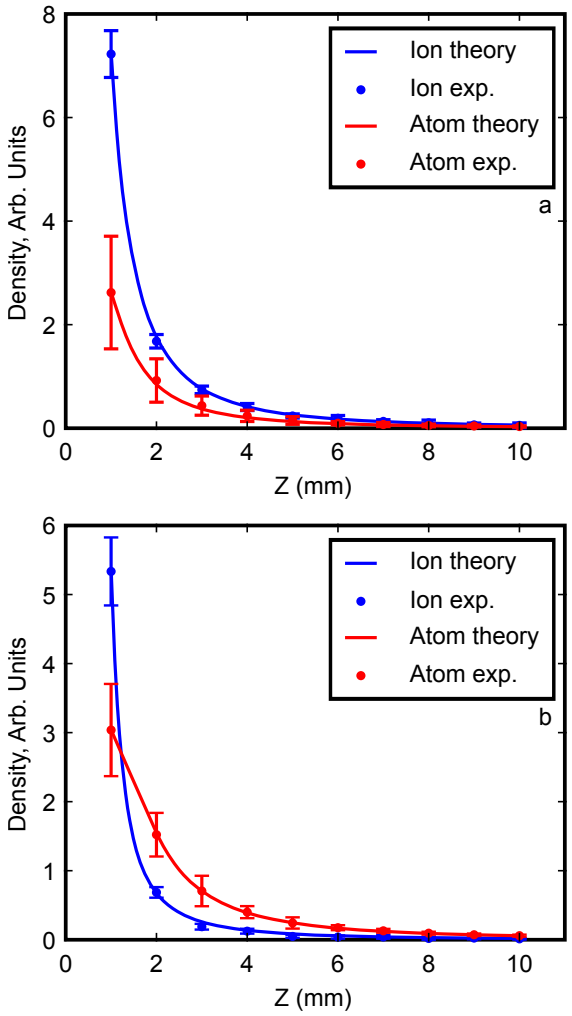

Figure 5.10 The geometry scaled experimental data vs the on-axis densities calculated using Eqs. 5.16 and (5.19). Plot (a) shows the results for 1100 W. Plot (b) shows the results for 700 W. The electron temperatures and densities used to calculate these values are in Figs. 5.11 and 5.12.

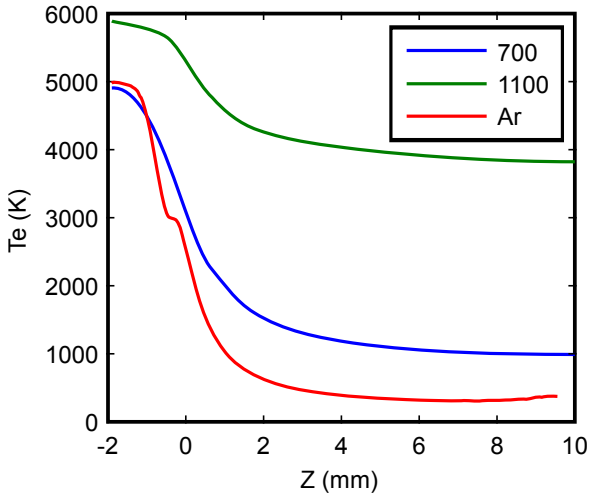

Figure 5.11 Electron temperatures used to create Fig. 5.10. The actual temperatures should match these within about 20%. "Ar" is the FENIX simulation argon neutral temperature plotted for reference. For this plot, FENIX was given an upstream temperature of 5000 K to simulate the cool central channel.

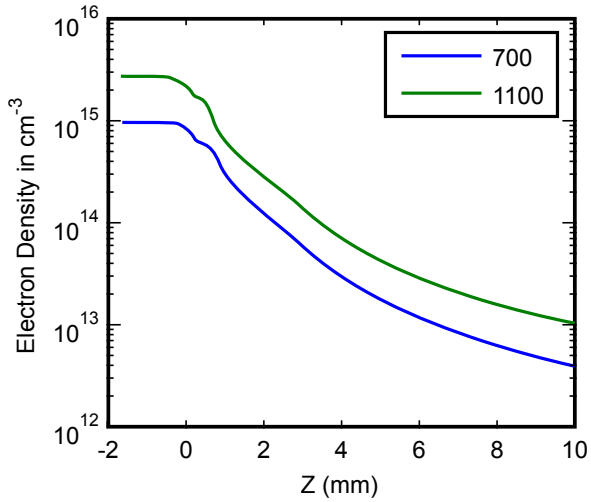

Figure 5.12 Electron densities used to create Fig. 5.10. The actual electron densities should match these within 50%.

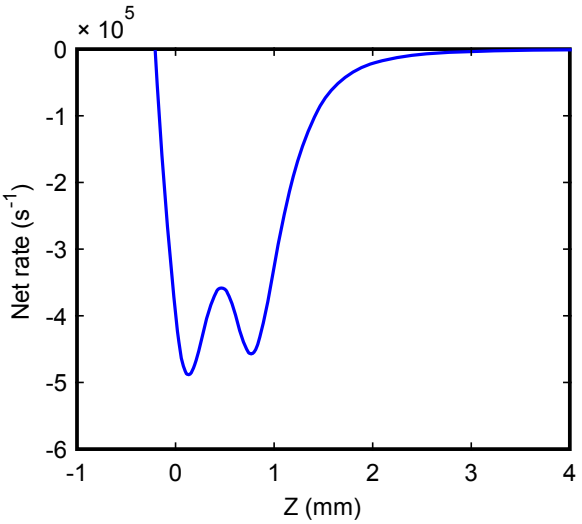

Figure 5.13 The net ionization/recombination rate, calculated using the electron temperature and density from Figs. 5.11 and 5.12. It assumes that $n_I \approx n_A$. While this is not necessarily true, n_I and n_A are the same order of magnitude, and the figure gives a good qualitative view of where recombination is occurring. Z=0 is set at the tip of the sampling cone.

more complicated. The extent of the experimental data does not warrant developing a solution to the coupled continuity equation that could extend the ion and atom densities further upstream. To allow for a qualitative discussion, Fig. 5.13 assumes that $n_I \approx n_A$. Though not necessarily true, they are the same order of magnitude and should give a good indication of the recombination/ionization rate's behavior.

Up until about half a millimeter upstream from the sampler tip, the analyte ionization rate is larger than the recombination rate. As a result, almost all of the analyte is ionized. While not shown in Fig. 5.13, more than 1 mm upstream from the tip of the sampling cone, ionization dominates and the analyte is mostly ionized. Moving downstream from $Z = -1$ mm (1 mm upstream from the sampling cone tip), the electron temperature begins to drop due to thermal contact with cold electrons in the adiabatic expansion of the free jet, and by about 0.5 mm upstream from the sampler tip recombination begins to win out over ionization. Recombination hits a maximum inside the

sampler throat where the electrons are cooling due to thermal contact with the downstream electrons, but the plasma has expanded very little, keeping the electron density relatively high. Once the analyte passes through the sampler, the combination of thermal contact with the upstream electrons keeping the electron temperature from decreasing too much, along with a quickly dropping electron density, shuts off recombination by two or three millimeters downstream from the sampler orifice. By that position, recombination is rare, and the ratio of ion to atom density stops changing.

Macedone's and Farnsworth's experimental data suggest that a hotter upstream electron temperature can greatly reduce the amount of recombination that occurs. However, increasing the temperature to create more ions also increases the number of doubly ionized analyte which in turn interferes with the analyte signal. Macedone and Farnsworth also used a sampler whose orifice was about half a millimeter long. Shortening the length of the sampler orifice may reduce the amount of time the analyte ions spend in the high recombination zone in the sampler throat, improving transmission.

5.5 Conclusion

Using FENIX and the continuity equation, an approximate electron density and temperature have been calculated for the first vacuum stage when using 700 W or 1100 W of incident power. Using FENIX in conjunction with Macedone's and Farnsworth's experimental data has also led to the calculation of the ion to atom ratios at that power.

Also, by using Stevefelt's recombination rate, theoretical calculations have been able to roughly reproduce Macedone's and Farnsworth's experimental data.

It appears from the data that at the higher incident power, not only are more ions ionized, but fewer recombine while traveling through the sampler, resulting in a larger ion signal.

Bibliography

[1] D. J. Douglas and J. B. French, "Gas dynamics of the inductively coupled plasma mass spectrometry interface," J. Anal. At. Spectrom. **3,** 743–747 (1988).

[2] R. L. Spencer, J. Krogel, J. Palmer, A. Payne, A. Sampson, W. Somers, and C. N. Woods, "Modeling the gas flow upstream and in the sampling nozzle of the inductively coupled plasma mass spectrometer via the Direct Simulation Monte Carlo algorithm," Spectrochimica Acta Part B: Atomic Spectroscopy **64,** 215–221 (2009).

[3] P. B. Farnsworth, R. L. Spencer, W. N. Radicic, N. Taylor, J. Macedone, and H. Ma, "A comparison of ion and atom behavior in the first stage of an inductively coupled plasma mass spectrometer vacuum interface: Evidence of the effect of an ambipolar electric field," Spectrochimica Acta Part B: Atomic Spectroscopy **64,** 905 – 910 (2009).

[4] R. L. Spencer, N. Taylor, and P. B. Farnsworth, "Comparison of calculated and experimental flow velocities upstream from the sampling cone of an inductively coupled plasma mass spectrometer," Spectrochimica Acta Part B: Atomic Spectroscopy **64,** 921 – 924 (2009).

[5] A. Kantrowitz and J. Grey, "A High Intensity Source for the Molecular Beam. Part I. Theoretical," Review of Scientific Instruments **22,** 328–332 (1951).

[6] G. B. Kistiakowsky and W. P. Slichter, "A High Intensity Source for the Molecular Beam. Part II. Experimental," Review of Scientific Instruments **22,** 333–337 (1951).

[7] P. L. Owen and C. K. Thornhill, "The flow in an axially-symmetric supersonic jet from a nearly-sonic orifice into a vacuum," Aeronautical Research Council Reports and Memoranda (1948).

[8] H. Ashkenas and F. S. Sherman, "Structure and utilization of supersonic free jets in low density wind tunnels," in *4th RGD* (1966), Vol. 2, p. 784.

[9] J. W. Brook and R. A. Oman, in *IVth Symposium of Rarefied Gas Dynamics*, J. M. de Leeuw, ed., (Academic, New York, 1965), Vol. 1, p. 129.

[10] P. L. Bhatnagar, E. P. Gross, and M. Krook, "A Model for Collision Processes in Gases. I. Small Amplitude Processes in Charged and Neutral One-Component Systems," Phys. Rev. **94,** 511–525 (1954).

[11] B. B. Hamel and D. R. Willis, "Kinetic Theory of Source Flow Expansion with Application to the Free Jet," Physics of Fluids **9,** 829–841 (1966).

[12] E. L. Knuth and S. S. Fisher, "Low-Temperature Viscosity Cross Sections Measured in a Supersonic Argon Beam," The Journal of Chemical Physics **48,** 1674–1684 (1968).

[13] D. Miller and R. Andres, *VIth Symposium of Rarefied Gas Dynamics* (Academic Press, New York, 1969), Vol. 2, p. 1385.

[14] J. P. Toennies and K. Winkelmann, "Theoretical studies of highly expanded free jets: Influence of quantum effects and a realistic intermolecular potential," The Journal of Chemical Physics **66,** 3965–3979 (1977).

[15] D. Douglas, in *Analytical Atomic Spectrometry*, 2nd ed., A. Monaster and D. Golightly, eds., (VCH, New York, 1991).

[16] A. A. Mills, J. H. Macedone, and P. B. Farnsworth, "High resolution imaging of barium ions and atoms near the sampling cone of an inductively coupled plasma mass spectrometer," Spectrochimica Acta Part B: Atomic Spectroscopy **61,** 1039 – 1049 (2006).

[17] J. H. Macedone and P. B. Farnsworth, "Changes in plasma composition during the expansion into the first vacuum stage of an inductively coupled plasma mass spectrometer," Spectrochimica Acta Part B: Atomic Spectroscopy **61,** 1031 – 1038 (2006).

[18] B. S. Duersch, Y. Chen, A. Ciocan, and P. B. Farnsworth, "Optical measurements of ion density in the second vacuum stage of an inductively coupled plasma mass spectrometer," Spectrochimica Acta Part B: Atomic Spectroscopy **53,** 569 – 579 (1998).

[19] G. Bird, *Molecular gas dynamics and the direct simulation of gas flows* (Clarendon Press, Oxford, 1994).

[20] H. Ellis, R. Pai, E. McDaniel, E. Mason, and L. Viehland, "Transport properties of gaseous ions over a wide energy range," Atomic Data and Nuclear Data Tables **17,** 177 – 210 (1976).

[21] H. Ellis, E. McDaniel, D. Albritton, L. Viehland, S. Lin, and E. Mason, "Transport properties of gaseous ions over a wide energy range. Part II," Atomic Data and Nuclear Data Tables **22,** 179 – 217 (1978).

[22] H. Ellis, M. Thackston, E. McDaniel, and E. Mason, "Transport properties of gaseous ions over a wide energy range. Part III," Atomic Data and Nuclear Data Tables **31,** 113 – 151 (1984).

[23] L. Viehland and E. Mason, "Transport Properties of Gaseous Ions over a Wide Energy Range, IV," Atomic Data and Nuclear Data Tables **60,** 37 – 95 (1995).

[24] K. Koura and H. Matsumoto, "Variable soft sphere molecular model for inverse-power-law or Lennard-Jones potential," Physics of Fluids A: Fluid Dynamics **3,** 2459–2465 (1991).

[25] K. Koura and H. Matsumoto, "Variable soft sphere molecular model for air species," Physics of Fluids A: Fluid Dynamics **4,** 1083–1085 (1992).

[26] W. N. Radicic, J. B. Olsen, R. V. Nielson, J. H. Macedone, and P. B. Farnsworth, "Characterization of the supersonic expansion in the vacuum interface of an inductively coupled plasma mass spectrometer by high-resolution diode laser spectroscopy," Spectrochimica Acta Part B: Atomic Spectroscopy **61,** 686 – 695 (2006).

[27] J. H. MacEdone, A. A. Mills, and P. B. Farnsworth, "Optical measurements of ion trajectories through the vacuum interface of an inductively coupled plasma mass spectrometer," Applied spectroscopy **58,** 463–467 (2004).

[28] T. Boyd and J. Sanderson, *The Physics of Plasmas* (Cambridge University Press, 2003), pp. 300–301.

[29] G. Gamez, S. A. Lehn, M. Huang, and G. M. Hieftje, "Effect of mass spectrometric sampling interface on the fundamental parameters of an inductively coupled plasma as a function of its operating conditions: Part I. Applied r.f. power and vacuum," Spectrochimica Acta Part B: Atomic Spectroscopy **62,** 357 – 369 (2007).

[30] F. Chen, *Introduction to Plasma Physics and Controlled Fusion*, No. v. 1 in *Introduction to Plasma Physics and Controlled Fusion* (Springer, 1984), pp. 290–295.

[31] T. Sheridan and J. Goree, "Collisional plasma sheath model," Physics of Fluids B: Plasma Physics (1989-1993) **3,** 2796–2804 (1991).

[32] R. Houk, J. K. Schoer, and J. S. Crain, "Plasma potential measurements for inductively coupled plasma mass spectrometry with a centre-tapped load coil," Journal of Analytical Atomic Spectrometry **2,** 283–286 (1987).

[33] H. Niu and R. Houk, "Langmuir probe measurements of the ion extraction process in inductively coupled plasma mass spectrometry-I. spatially resolved determination of electron density and electron temperature," Spectrochimica Acta Part B: Atomic Spectroscopy **49,** 1283 – 1303 (1994).

[34] R. Fraser, F. Robben, and L. Talbot, "Flow properties of a partially ionized free jet expansion," Physics of Fluids (1958-1988) **14,** 2317–2327 (1971).

[35] H. Lim, R. Houk, M. Edelson, and K. P. Carney, "Some fundamental characteristics of a reduced-pressure plasma extracted from an inductively coupled plasma," Journal of Analytical Atomic Spectrometry **4,** 365–370 (1989).

[36] D. Beauchemin, J. McLaren, and S. Herman, "Study of the effects of concomitant elements in inductively coupled plasmamass spectrometry," Spectrochimica Acta Part B: Atomic Spectroscopy **42,** 467–490 (1987).

[37] D. Douglas and J. French, "An improved interface for inductively coupled plasma-mass spectrometry (ICP-MS)," Spectrochimica Acta Part B: Atomic Spectroscopy **41,** 197–204 (1986).

[38] R. Houk and N. Praphairaksit, "Dissociation of polyatomic ions in the inductively coupled plasma," Spectrochimica Acta Part B: Atomic Spectroscopy **56,** 1069–1096 (2001).

[39] J. H. Macedone, D. J. Gammon, and P. B. Farnsworth, "Factors affecting analyte transport through the sampling orifice of an inductively coupled plasma mass spectrometer," Spectrochimica Acta Part B: Atomic Spectroscopy **56,** 1687–1695 (2001).

[40] J. H. Macedone and P. B. Farnsworth'.

[41] J. Stevefelt, J. Boulmer, and J. F. Delpech, "Collisional-radiative recombination in cold plasmas," Phys. Rev. A **12,** 1246–1251 (1975).

[42] J. D. Huba, "Naval Research Laboratory Plasma Formulary, revised," (2011).

[43] A. Müller and A. Wolf, "Production of antihydrogen by recombination of $\bar{p}$ with e^+: What can we learn from electron–ion collision studies?," Hyperfine Interactions **109,** 233–267 (1997).